

# We are IntechOpen, the world's leading publisher of Open Access books Built by scientists, for scientists

6,900

Open access books available

186,000

International authors and editors

200M

Downloads

Our authors are among the

154

Countries delivered to

TOP 1%

most cited scientists

12.2%

Contributors from top 500 universities



WEB OF SCIENCE™

Selection of our books indexed in the Book Citation Index  
in Web of Science™ Core Collection (BKCI)

Interested in publishing with us?  
Contact [book.department@intechopen.com](mailto:book.department@intechopen.com)

Numbers displayed above are based on latest data collected.  
For more information visit [www.intechopen.com](http://www.intechopen.com)



# Passive Microwave Feed Chains for High Capacity Satellite Communications Systems

Giuseppe Addamo, Oscar Antonio Peverini,  
Giuseppe Virone and Riccardo Tascone  
*IEIIT - CNR Torino,  
Italy*

## 1. Introduction

The successful implementation of satellite communication systems requires robust wireless channels providing the up-links and down-links for the communication signals. The frequency operative bands employed depend on the particular application. Navigation and mobile satellite systems are typically operated in the L (1-2 GHz) and S (2-4 GHz) bands, whereas remote-sensing applications are mostly offered in C (4-8 GHz) band. In the commercial communication area, due to the increasing demand of high quality services, the operating frequency bands has evolved towards the Ku (12-18 GHz), K (19-21 GHz) and Ka (27-32 GHz) bands. Although communication systems operating in high frequency bands provide more channel capacity, the effect of free-space attenuation and atmospheric absorption can limit the performances of these systems (e.g. signal-to-noise ratio). In this contest, the employment of efficient transmission algorithms and protocols provide meaningful advantages, but the bottle-neck is however represented by the antenna system that has to satisfy very strict requirements. For these reasons each device composing the antenna-feed chain has to be designed in order to guarantee significant electromagnetic performances and, at the same time, high integration levels (Cecchini et al., 2009). Moreover, when high power levels are employed (also of the order of tens of KW), further problems are related to spurious interferences generated by non-linear devices, as microwave amplifiers, and by metallic contacts that behave as a diode junction due to the oxidation of the metals. Additionally, high-power and low-pressure conditions can cause multipaction discharges in the devices (Addamo et al., 2010). This phenomenon is an exponential growth of electrons emitted by the metallic surfaces due to the synchronism between the applied electromagnetic field and the free electrons inside the components. The final effect consists in the damage and even in the destruction of the RF device.

## 2. Antenna-feed system architecture

The most general architecture of a dual-band dual-polarization antenna-feed system is shown in Fig. 2.1, where the paths covered by both the transmitter signals (in blue) and the receiver signals (in red) are reported. The same antenna is employed in both the transmitting (Tx) and receiving (Rx) mode, since the transmitters and the receivers works on different frequency bands (Harwanger et al., 2007), (Cecchini et al., 2009). By considering

the system in the transmitting mode, the two separate microwave sources generate two independent signals. These are combined by the ortho-mode transducer (OMT) (Peverini et al., 2009) to obtain two orthogonal linear polarizations in a common waveguide connected to the antenna-feed. If circular polarizations are required, then a polarizer is introduced between the OMT and the antenna-feed in order to convert the incoming linearly-polarized signals into left- and right-hand polarizations (Virone et al., 2008). Finally, the antenna-feed radiates the Tx signals onto the reflector system.

In the receiving mode, the two circularly-polarized signals collected by the feed are converted by the polarizer into two linear orthogonal ones. The OMT separates these two orthogonal linear polarizations by routing them into two different single-polarization channels. Subsequently, the signals are amplified by low-noise amplifiers (LNAs), and elaborated by the back-end electronic of the receiver. Since the Rx and Tx signals are allocated in different frequency bands, they can coexist in the first stages of the chain without interfering each other. The diplexers allow the separation of these signals by routing them in different paths as a function of the frequency (Virone et al., 2009). In order to protect the receivers from spurious interfering signals generated by both internal and external transmitters operating in different frequency bands, various stop-band filters are inserted in the chain. Moreover, the correct behaviour of this system requires high performances also in terms of polarization purity. For this purpose, usually a corrugated horn is employed as the antenna-feed for its significant performances in terms of wide band and low cross-polarization levels (Addamo et al., 2009), (Beniguel et al., 2005).

An overview on the passive waveguide devices composing this chain (i.e. filters, diplexers, OMTs, and feed-horns) is reported in the next sessions, focusing on the main issues and characteristics (i.e. power-handling capability), and on the design techniques.

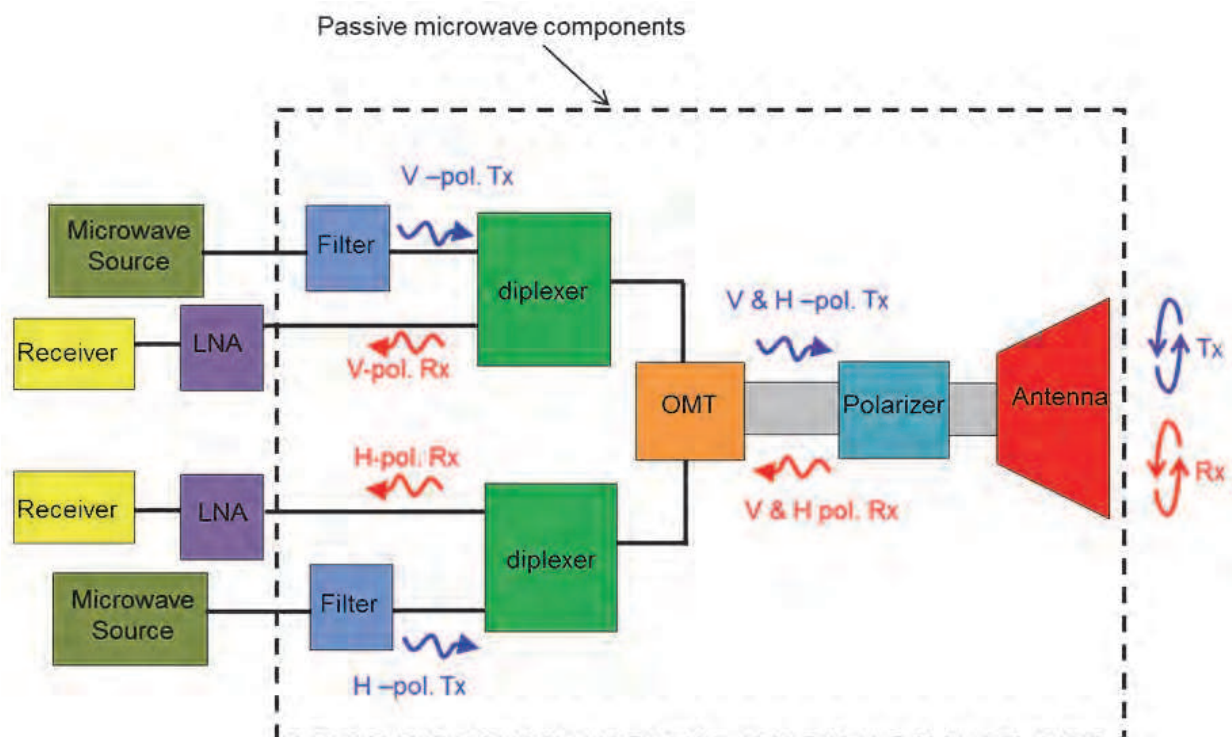


Fig. 2.1. General architecture of a dual-band dual-polarization antenna-feed system for satellite communication.

### 3. Multipactor discharge and passive intermodulation products

The trend in modern communication satellites is to increase the number of channels that can be handled by each RF payload in order to both minimize the mass, volume, and cost of satellites and to increase the reconfigurability flexibility of these communication systems. As an example, dual-band and tri-band RF chains operating in multi-carrier condition are currently adopted in several satellite programs for broadcast and fixed services in Ku, K, Ka-bands (Cecchini, et al., 2010). Consequently, the RF peak-power supplied to the antenna feed-systems can reach tens of kW. When such levels of power are employed, spurious unwanted phenomena can occur inside the components that can concretely damage or limit the operative function of the entire antenna-feed system. The most considerable ones are the multipactor discharge phenomenon and the generation of passive intermodulation products (PIMPs).

#### 3.1 Multipactor discharge

Multipactor discharge is a breakdown mechanism that can occur under high-power and low-pressure conditions when a proper synchronism condition between the applied electromagnetic (EM) field and free electrons inside the components is met. Indeed, free electrons in microwave devices operating at low-pressure conditions can be accelerated by the applied EM field and impact onto the metallic internal surfaces. This impact can generate additional electrons by secondary emission that in turn can strike other surfaces. If appropriate dynamical conditions are satisfied, these repeated collisions and emissions can lead to an exponential growth of electrons and a subsequent discharge, thus increasing the noise level and modifying the electric parameters of the devices. Since the multipactor breakdown phenomenon sets severe constraints on the power level that can be handled by satellite payloads, specific device architectures are needed in order to overcome this problem. In particular, it is highly recommended that the design of each component satisfies suitable confidence margins with respect to multipaction discharge so that time- and cost-expensive experimental high-power testing can be avoided in the qualification process of the payloads. The multipactor breakdown phenomenon is based on a resonance condition that can arise when the electron mean free path (i.e. the average distance covered by a moving particle between successive collisions) is greater than the distance between two opposite metallic surfaces. Moreover, two additional conditions are needed. The first one is related to the impact time between two subsequent collisions onto the metallic surfaces. Under a single-carrier condition, this parameter has to be an odd number  $M$  of half cycles of the applied EM signal. The second condition implies that the arrival electron energy onto the metallic surface is sufficiently considerable so that the effective secondary emission ratio  $\delta$  is greater than one. The latter coefficient depends also on the electrons incident angle, the surface material (typically aluminum), and the coating process applied to the metallic surfaces (e.g. silver-plating, alodine coating).

In order to gain a physical insight into the multipactor discharge phenomenon, it is useful to consider the simple model of a free electron in a plane parallel-plate waveguide where an electric field with TEM modal voltage  $V(t) = V_0 \sin \omega t$  is present (see Fig. 3.1). The motion equation for an electron of mass  $m$  and charge  $e$  is

$$m\ddot{x}(t) = \frac{e}{d} V_0 \sin \omega t \quad (1)$$

together with the initial condition  $\dot{x}(t_0) = v_0$  and  $x(t_0) = 0$ . If an electron is released from surface  $x=0$  with velocity  $v_0$ , then integration of Eq. (1) yields the velocity from which the position can be derived as

$$\dot{x}(t) = \frac{e}{md} \frac{V_0}{\omega} (\cos \alpha - \cos \omega t) + v_0 \quad (2)$$

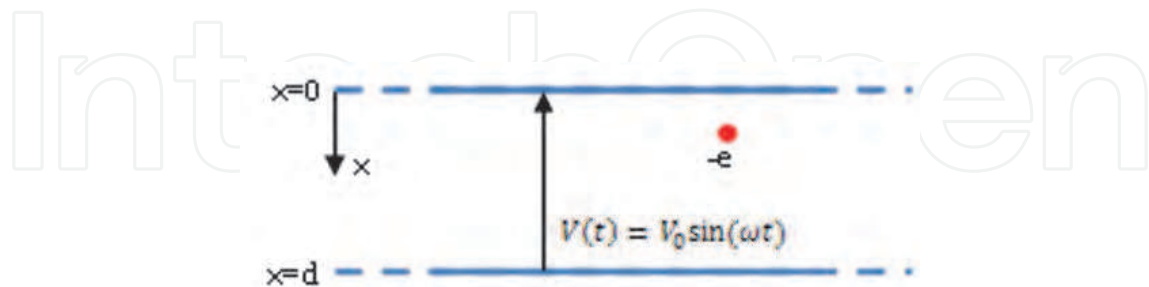


Fig. 3.1. Plane parallel-plate waveguide under consideration for the analysis of the multipaction breakdown phenomenon.

$$x(t) = \frac{e}{md} \frac{V_0}{\omega^2} ((\omega t - \alpha) \cos \alpha - \sin \omega t + \sin \alpha) + \frac{v_0}{\omega} (\omega t - \alpha) \quad (3)$$

where  $\alpha = \omega t_0$ . In order the transit time  $\Delta t$  to the position  $x=d$  to be an odd number  $M$  of half cycles (i.e.  $\Delta t = M\pi / \omega$ ), the peak voltage  $V_0$  of the EM field and the electron impact velocity  $v_i$  must be equal to

$$V_0 = \frac{m}{e} \frac{\omega d (\omega d - M\pi v_0)}{M\pi \cos \alpha + 2 \sin \alpha} \quad (4)$$

$$v_i = \frac{2e}{m} \frac{V_0}{\omega d} \cos \alpha + v_0 \quad (5)$$

respectively. According to Eq. (4) the value of the peak voltage  $V_0$  fulfilling the synchronism condition (named also the multipactor threshold voltage) depends on  $\alpha$  (i.e. the time  $t_0$  when the electrons are released from the surface  $x=0$ ) and on the gap-frequency product (i.e.  $fd$ ). With reference to Eq. (5), it is worth noting that the kinetic energy  $\frac{mv_i^2}{2}$  of the primary electron striking the surface  $x=d$  depends on the peak voltage  $V_0$ . If this energy is sufficiently high so that the secondary electron emission coefficient  $\delta$  of the surfaces is greater than one, than an electron avalanche phenomenon occurs between the two surfaces. On the basis of the previous theory, it is possible to derive the relationship between the gap-frequency product  $fd$  and the threshold voltage  $V_0$  for each odd-order resonance, thus obtaining useful design tools such as the Hatch-Williams susceptibility diagrams. The latter are the basis of the free multipactor calculator program developed by the European Space Agency and available online (ESA, 2007), which provides the region in the  $fd - V_0$  plane where the multipaction breakdown can occur for a given resonance order. Fig. 3.2 shows the envelope over all the resonance orders of the minimum threshold voltage for a silver-plated

parallel-plate waveguide. It is worth mentioning that since the EM field inside a generic component can deviate significantly from the TEM field in a plane parallel-plate waveguide, the rigorous analysis of the multipaction breakdown would require extensive numerical computations of the electronic trajectories inside the devices in order to establish if an avalanche of secondary-emission electrons can occur (Anza, et al., 2008)-(Tienda, et al, 2006).

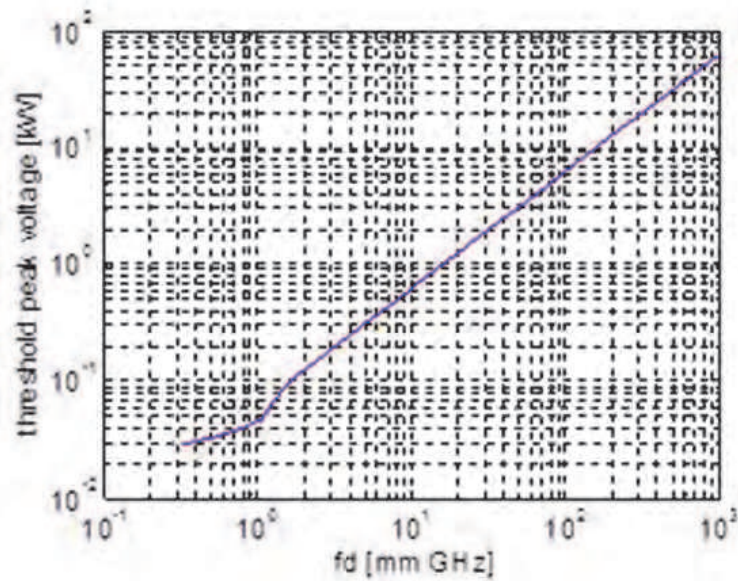


Fig. 3.2. Envelope over all the resonance order of the minimum multipactor threshold voltage  $V_0$  as a function of the gap-frequency product  $fd$  for a silver-plated parallel-plate waveguide.

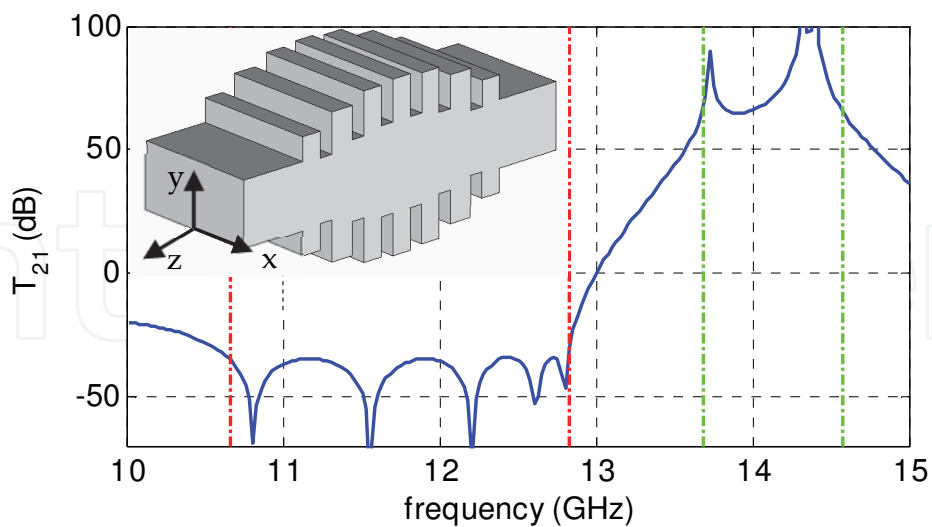


Fig. 3.3. Transmission coefficient  $T_{21}(f)$  of the E-plane WR75-waveguide symmetric stub-filter shown in the insert (the inside waveguide structure of the filter is reported).

However, according to the ESA recommendations, the qualification process of a generic RF component in terms of the power-handling under both single- and multi-carrier operating

conditions can be carried out by evaluating an upper-bound on the multipaction risk and setting appropriate confidence margins. In particular, the actual upper-bound is computed by using the plane parallel-plate model along several directions inside the component. For sake of clarity and without loss of generality, this procedure is described next by referring to the E-plane WR75-waveguide symmetric stub-filter depicted in the insert of Fig. 3.3, where the transmission coefficient  $T_{21}(f)$  of this filter is reported. The transmission coefficient is the relevant characteristic function of the filter, since it is equal to the ratio  $S_{11}(f)/S_{21}(f)$  where  $S_{11}(f)$  is the scattering reflection coefficient at the input port, and  $S_{21}(f)$  is the scattering transmission coefficient from one port to the other. Hence, the transmission coefficient  $T_{21}(f)$  is proportional to the reflection coefficient in the pass-band and to the inverse of the transmission between the two ports in the stop-band (isolation). The E-plane stub architecture is commonly adopted in the Tx-channels of multiplexers (Tx-band = [10.7, 12.75] GHz) to block the Rx signals (Rx-band = [13.5, 14.5] GHz), since each stub exhibits a transmission zero that can be adjusted in the stop-band by varying its length. In this way, high levels of isolation can be achieved in the Rx-band along with very low standing-wave ratio inside the component in the Tx-band. The latter condition can be exploited in order to maximize the power-handling capability of these components.

Since this filter is an E-plane structure, the maximum electric field arises in the central plane  $x=0$ , for which the in-phase field lines at 13 GHz are depicted in Fig. 3.4. Although the field in the device is not everywhere oriented along straight lines connecting two parallel surfaces (as in the parallel-plate model), it is possible to define a parallel-plate model for each of the lines highlighted in cyan in Fig. 3.4. For this propose, the equivalent voltage

$$V_i(f) = \int_0^{d_i} \underline{E}(s; f) \cdot \hat{s} ds \quad (6)$$

is evaluated on the  $i$ -th integration line (oriented along  $\hat{s}$ ). Moreover, the corresponding multipaction threshold voltage  $V_i^{(thres)}$  for this section of the device, can be evaluated in terms of the frequency-gap product  $fd_i$  by means of the susceptibility diagrams. For design purposes, it is useful to introduce the voltage magnification factor  $VMF_i$  (Parikh, et al., 2003) that provides a measure of the magnification of the electrical field occurring in the  $i$ -th position referred to the incident voltage  $V^{(inc)}$

$$VMF_i(f) = \frac{V_i(f)}{V^{(inc)}} \quad (7)$$

Accordingly, a breakdown-free condition is guaranteed at the  $i$ -th section of the device if the input power is smaller than the threshold level

$$P_i(f) = \frac{|V_i^{(thres)}|^2}{2Z^{(inc)} |VMF_i|^2} \quad (8)$$

where  $Z^{(inc)}$  is the power-voltage impedance at the input waveguide port. Finally, the overall breakdown threshold power of the device at frequency  $f$  is

$$P^{(SC)}(f) = \min_i \{P_i(f)\} \quad (9)$$

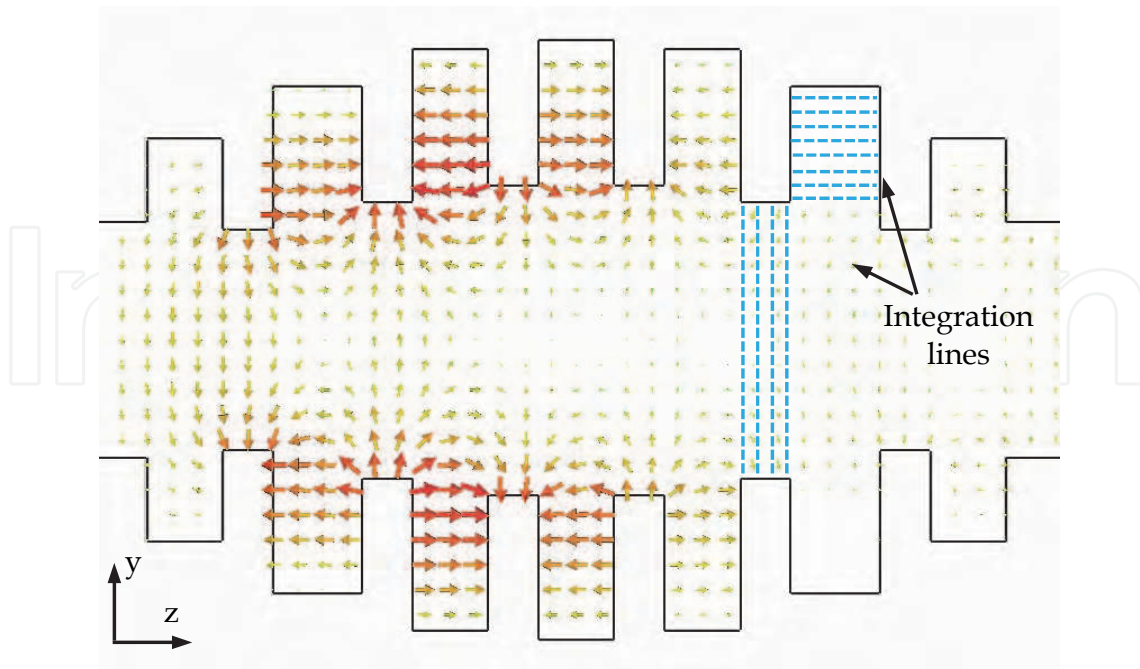


Fig. 3.4. In-phase field lines in the plane  $x=0$  of the E-plane WR75-waveguide symmetric stub-filter shown in the insert of Fig. 3.3. The frequency is equal to 13 GHz. The lines highlighted in cyan correspond to the integration lines used to define the equivalent parallel-plate models.

that clearly defines the power-handling capability of the component in a single-carrier regime. Fig. 3.5 reports the frequency behavior of  $P^{(SC)}(f)$  for the E-plane stub-filter in the Tx-band. The minimum value of 2.6 kW at 12.75 GHz is due to the high levels of standing-waves that are established inside the stubs at frequencies close to the -3 dB cut-off frequency, in order to achieve high levels of isolation in the stop-band [13.5, 14.5] GHz. In this regard, the power-handling capability of any device can be increased by adopting the following strategies:

- Enlargement of the design bandwidth with respect to the actual operating bandwidth of the device. In this way, as stated previously, the power-handling capability is not adversely affected by very high standing-waves inside the component towards the band limits.
- Application of surface-coating processes (i.e. silver-plating), since they guarantee higher breakdown threshold voltages with respect to bare aluminum. It is worth mentioning that the choice of the specific surface treatment has to be made by considering both the insertion loss and the power-handling requirements.
- Setting proper constraints on the geometric parameters during the design of the architecture. Indeed, a significant improvement in the power-handling capability can be achieved by varying the height of the most critical sections of the component under analysis. This leads to a larger frequency-gap product and, consequently, to higher value of breakdown voltages. Hence, the geometrical parameters of the architecture are determined through a trade-off process between the electrical requirements (e.g. return-loss at the input ports or channel isolation) and the power-handling capability of the

device. In this view, the design of novel instrumentation architectures exhibiting very good electrical figure-of-merits along with very high power-handling capabilities is a cutting-edge research topic for satellite communication systems.

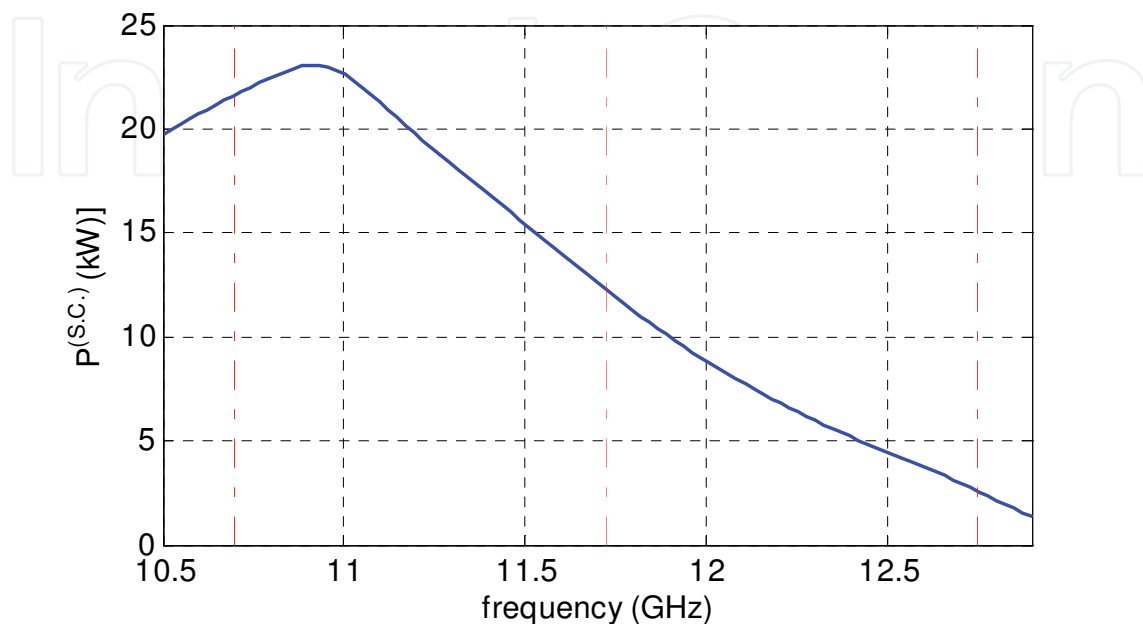


Fig. 3.5. Single-carrier breakdown threshold power  $P^{(SC)}(f)$  for the E-plane WR75-waveguide symmetric stub-filter shown in the insert of Fig. 3.3.

On the basis of the single-carrier analysis previously described, it is possible to derive the relevant design upper-bounds on the maximum power deliverable to the device operating in a multi-carrier condition. Under the assumption of  $N$  carriers with equal power  $P$ , the worst case corresponds to the in-phase sum of the carrier fields, thus leading to a total peak-power equal to  $N^2P$ . As a consequence, the breakdown-free condition in the device is certainly guaranteed if the input power per carrier  $P$  is smaller than the threshold level

$$P^{(MC)} = \frac{1}{N^2} \min_f \{P^{(MC)}(f)\} \quad (10)$$

By considering a further margin of 3 or 6 dB, the standardized " $N^2 \cdot P + 6$  dB" or " $N^2 \cdot P + 3$  dB" rules are derived. Actually, these upper-bounds provide to be too strict when a high number of carriers are considered. Indeed, the in-phase condition of the  $N$  carriers can be satisfied only for a short span of time. Moreover, the multipactor breakdown is an electron secondary-emission resonance that has to be sustained by the applied EM field. For these reasons, the in-phase matching condition becomes critical for the multipactor breakdown only if it is satisfied for long time scales. In this respect, the high-power qualification process of the devices operating in a multi-carrier regime is usually carried out by adopting the more realistic "20-gap crossing" rule. The latter states that "as

long as the duration of the multi-carrier peak and the mode order gap are such that no more than 20 gap-crossings can occur during the multi-carrier peak, the design may be considered safe with regards to the multipaction breakdown even though the multipaction threshold may be exceeded from time to time". Implementation of this rule in the case of  $N$  linearly-spaced carriers (frequency spacing  $\Delta f$ ) yields the definition of the boundary function (Parikh, et al., 2003).

$$E_V = -(\sqrt{N} - 1) \ln\left(\frac{T_{20}}{T_H}\right) + \sqrt{N} \quad \text{for} \quad \sqrt{N} < E_V < N \quad (11)$$

where  $T_H$  is the period of multi-carrier envelope ( $T_H = 1 / \Delta f$ ) and  $T_{20}$  is the time taken by the electrons to cross the most critical gap 20 times. The latter parameter is equal to  $T_{20} = (20 \times n) / (2 \times f_0)$ , where  $n$  is the resonance order fulfilling the synchronism condition and  $f_0$  is the lower frequency in the band of interest. On the basis of this boundary function, the maximum power per carrier satisfying to the "20-gap crossing" is

$$P^{(MC)} = \frac{1}{E_V^2} \min_f \{P^{(MC)}(f)\} \quad (12)$$

to which a further 6 dB confidence margin is commonly added, thus defining the "20-gap crossing + 6 dB" rule. As an example, when considering 10 carriers linearly spaced in the Tx-band of the E-plane stub filter, the maximum power per carrier according to this rule is approximately 67 W.

### 3.2 Passive intermodulation products

Nonlinear characteristics in microwave components can lead to the generation of spurious passive intermodulation products (PIMPs). When the intermodulation products of two or more signals mixed in the device fall into the operative bandwidth of the receiver, this intermodulation signal becomes an interference problem (Lui, 1990). As an example, if two carriers with frequencies  $f_1$  and  $f_2$  propagate through a nonlinear passive component, the spurious intermodulation products are harmonics with frequencies  $f_{m,n} = mf_1 + nf_2$  with  $m, n$  integers. The sum  $|m| + |n|$  defines the order of the intermodulation product and the amplitude of the PIMPs rapidly decay as a function of the order  $|m| + |n|$ . However, for the case of considerable input power, some of the higher-order products can be great enough to cause serious interference problems. This usually happens in satellite communication systems where high-power transmitters and low-noise receivers are employed in the same antenna-feed system. As a consequence, appropriate counter-measures have to be taken in order to avoid the decrease of the signal-to-noise ratio in the Rx channels, which in turn reduces the receivers sensibility. As an example, PIMPs level as low as -140 dB are commonly required in Ku, K, Ka-band payloads operating broadcast and fixed satellite services.

Generation of PIMPs take place mainly in the Tx power-amplifier circuits, in the receiver mixers, and in the nonlinear metallic contacts inside the antenna-feed systems. The effects of PIMPs generated in the back-end circuits (amplifiers and mixers) can be minimized by inserting ad-hoc filters. On the contrary, PIMPs generated by possible metallic-oxide-

metallic contacts arising in the metallic mating surfaces of the front-end system components are more troublesome. Indeed, depending on the specific position of the intermodulation surface inside the antenna-feed chain, PIMPs can even not be filtered out. In this regard, the level of PIMPs generated in an oxidized surface that mates two metallic blocks depends significantly on the current through the junction. For this reason, the electrical and mechanical designs of all the front-end components are strictly connected. Indeed, special attention has to be paid when splitting a component in several blocks and in the connection of the components.

With regards to the E-plane stub-filter described in Sec. 3.1, the clam-shell assembly shown in Fig. 3.6 is a mechanical implementation of this device that is optimized in terms of PIMPs generation. The device is halved in two blocks along the central plane  $x=0$ , thus allowing a milling manufacturing of the inside waveguide structure. Since the currents in the central plane  $x=0$  are oriented along the longitudinal  $z$ -direction, no currents cross the two mating surfaces, thus avoiding the generation of PIMPs. Finally, the PIMPs generated at the input port sections, where the filter is connected to the other components, are minimized by adopting a choke/plain joint consisting of a choke flange (applied to the filter) and a plain flange (applied to the connecting device).

Fig. 3.7 shows the contour plot of the magnetic field amplitude inside the choke/plain joint at 12.75 GHz. It is worth noting, that the magnetic field, hence the electric current, in the contact point between the two flanges (named also cold point) is minimized with an appropriate design of the resulting L-shaped radial stub. Moreover, the joint is designed to exhibit a return-loss as high as possible in the operating bands (as high as 40 dB).

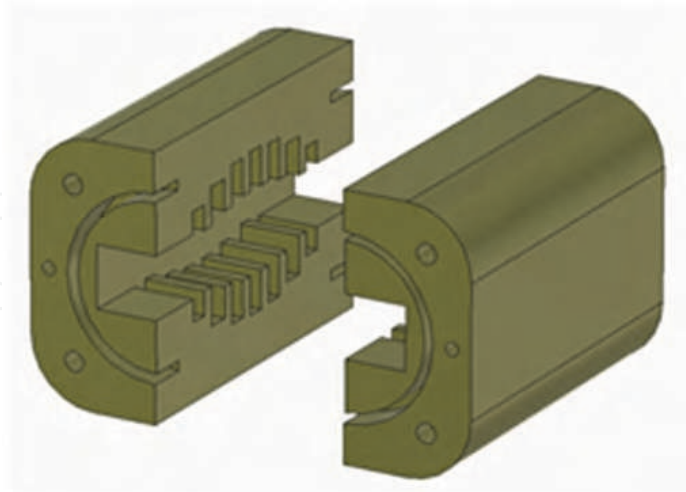


Fig. 3.6. Clam-shell mechanical assembly of the E-plane stub-filter shown in the insert of Fig. 3.3.

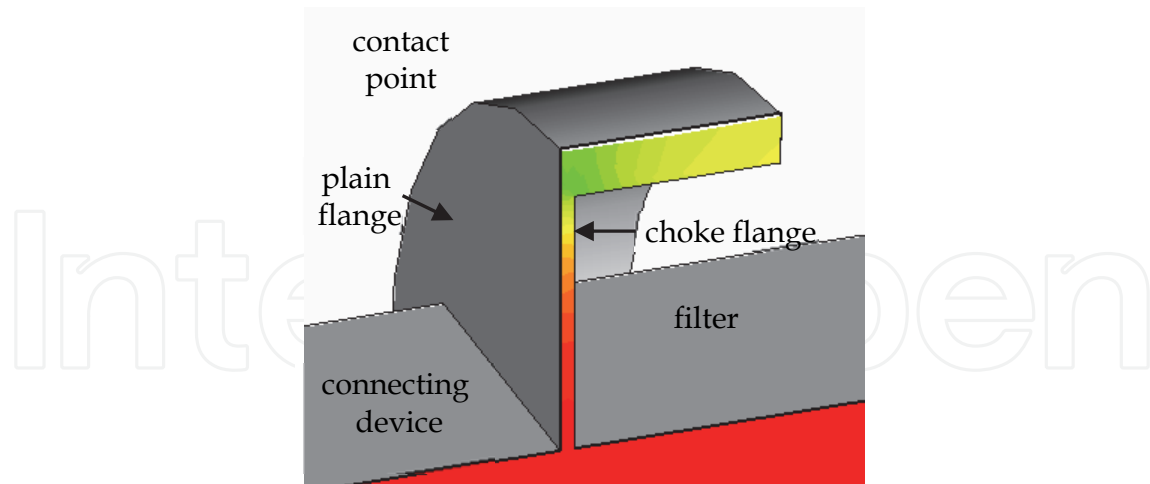


Fig. 3.7. Contour plot of the magnetic field inside the L-shaped radial stub resulting from the connection of the choke and plain flanges used to mount the filter of Fig. 3.6 with a connecting device (a rainbow contour scale is used).

#### 4. Broadband waveguide filters and diplexers

Metal waveguide filters are typically employed in satellite antenna-feed systems for their low losses and high power-handling at the microwave frequencies. As discussed in the introduction, these structures are mainly used to separate different sub-bands e.g. receive and transmit bands as well as to protect the source from spurious signals. The latter operation is usually performed using a single pass-band filter. The sub-band separation is instead performed using two (or more) filters in the diplexer (multiplexer) configuration. The same operation could be performed using a circulator, however, the diplexer solution exhibits high-performance and a low-cost.

A general diplexer configuration is sketched in Fig. 4.1, where two different filters (TX and RX) are connected to a three-port (T or Y) junction in order to obtain a common port (Port 1). The other filter ports are instead connected to proper waveguide transitions to provide the required orientation and size of Ports 2 and 3. More complex junctions could be adopted at port 1 in order to increase the number of sub-bands.

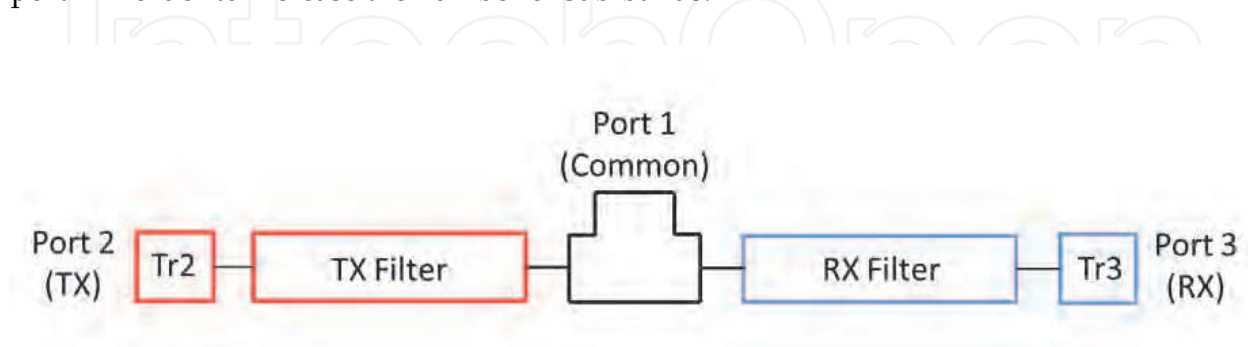


Fig. 4.1. Scheme of a waveguide diplexer.

With reference to the diplexer architecture in Fig. 4.1, the basic electrical requirements are a high transmission coefficient from Port 2 to Port 1, high attenuation from Port 2 to Port 3 and a low reflection coefficient at Port 2 in the TX frequency band. A high-transmission

coefficient from Port 1 to Port 3, a high attenuation from Port 1 to Port 2, and a low-reflection coefficient at port 3 have to be instead provided in the RX band. A low reflection coefficient at Port 1 for both frequency bands is also required.

It should be pointed out that filtering structures with relatively broad pass-bands (more than 5-10 %) are required owing to the present specifications of the satellite antenna feed systems. For this reason, specific synthesis techniques based on distributed parameter models and full-wave analysis tools should be adopted to design these kind of filters. These filters and their corresponding design procedures are hence very different with respect to narrow band (0.2-0.3 %) channel filters (not treated in this section) where the frequency dispersion of the discontinuities around the pass-band is practically negligible.

The filters for the antenna feed system duplexers can be designed according to either the pass-band or the stop-band architecture. Both of them can in principle be represented with the fundamental-mode equivalent circuit of Fig. 4.2.

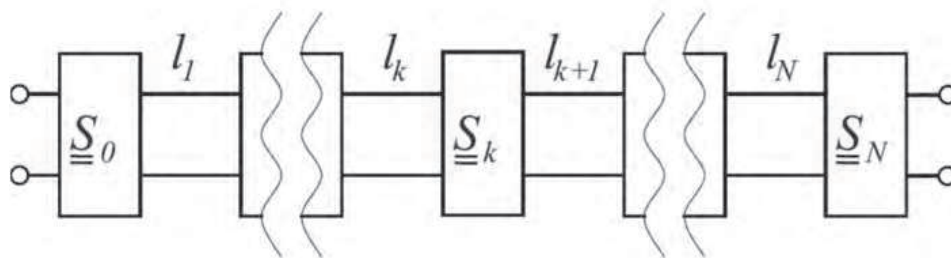


Fig. 4.2. Fundamental-mode transmission line equivalent circuit of a waveguide filter.

Such a circuit consists of  $N+1$  scattering matrices  $S_k$ , with  $k=0, \dots, N$ , connected by  $N$  transmission lines representing the same number of generic waveguide discontinuities and waveguide sections, respectively. The parameter  $l_k$  defines the length of these sections.

In pass-band architectures, the filtering behavior is mainly related to the phase rotation versus frequency in the  $N$  waveguide sections. In this framework, the latter are in fact usually referred as cavities or resonators. The main role of the discontinuities is instead to provide the required coupling between the adjacent resonators. However, as it will be discussed in the following, the spurious dispersive effect of the various discontinuities significantly affects the overall frequency behavior of the filter. Therefore, it should be kept into account in the design stage.

As far the stop-band architecture is concerned, the required transmission zeros are introduced by the discontinuities themselves, which exhibit a strong resonant behavior in this case. The spacing between the various discontinuities is instead adjusted to obtain a good matching in the pass-band.

The correct choice between the two architectures mainly depends on the overall required frequency behavior i.e. the width of the pass-, stop- and transition bands, the power handling capability, losses and the manufacturing complexity. Both the architectures will be discussed in the remainder of this section.

#### 4.1 Pass-band structures

Generally speaking, two class of discontinuities can be adopted in the design of pass-band filters. The first one is represented by the transverse discontinuities i.e. inductive (Rozzi, 1972) or capacitive irises (Virone, et al. 2007). A band-pass configuration with inductive (or

$H$ -plane) irises is shown in Fig. 4.3. As it can be seen, five resonators in rectangular waveguide are obtained owing to the presence of the six inductive irises. The peculiarity of this structure is the increased reflection coefficient of the irises at lower frequencies which lead to very high attenuation levels in the frequency region below the pass-band. The opposite phenomenon occurs with the capacitive configuration shown in Fig. 4.4. Indeed, the reflection coefficient of capacitive irises increases at higher frequency providing a very high attenuation above the pass-band of the whole filter. It has to be pointed out that waveguide resonators with an increased height (see Fig. 4.4) are used to reduce the overall losses.

For both the capacitive and inductive configurations, iris apertures and resonator lengths are the main design parameters. The iris thickness is generally selected according to the manufacturing materials and techniques. In particular, proper rounding of some of the filter corners is also required when milling machines are adopted. Nevertheless, this feature can be kept into account in modern design tools (Arndt, et al. 1997) in order to avoid the insertion of tuning screws.

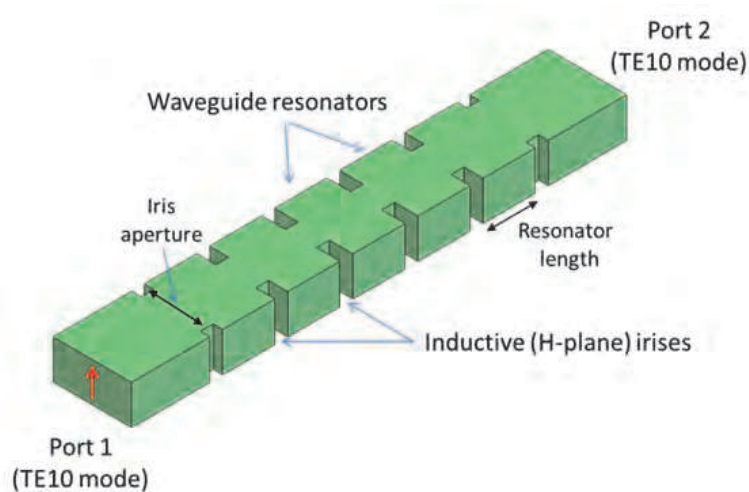


Fig. 4.3. Pass-band filter configuration with inductive ( $H$ -plane) irises.

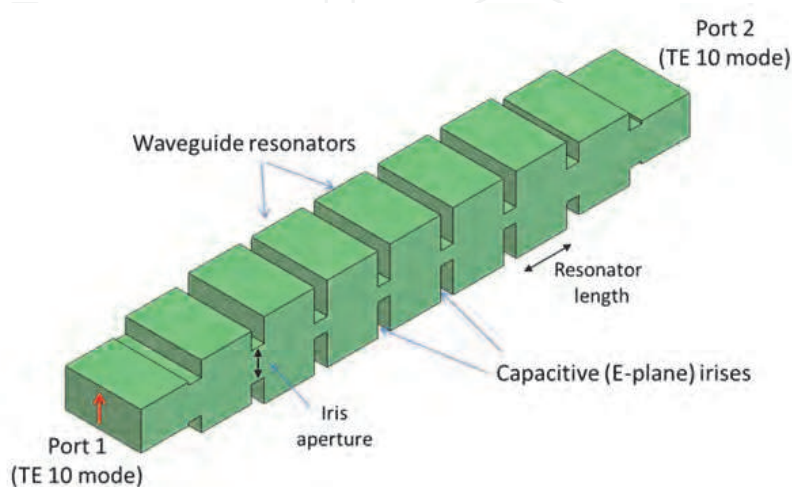


Fig. 4.4. Pass-band filter configuration with capacitive ( $E$ -plane) irises.

The second class of discontinuities for pass-band filters is represented by the longitudinal ones. Among these, the *E*-plane septum configuration shown in Fig. 4.5 is very popular (Vahldieck, et al, 1983). Such a discontinuity provides a very high reflection coefficient because the septum is placed in the middle of the waveguide where the electric field is maximum. Moreover, the electromagnetic field is evanescent in the septum region owing to the splitting of the main rectangular waveguide in two halves for which the TE<sub>10</sub> is below-cut off. The design parameters of the septum filter are both the resonator lengths and septum lengths. The septum width is usually selected according to manufacturing considerations. It should be pointed out that the septum reflection coefficient can even be too high for certain broadband applications. Therefore, open septa can be adopted as first and last discontinuities (Peverini, 2004). More advanced configurations feature ridge waveguide resonators, instead of the common rectangular ones, in order to decrease the overall length of the filter (Goussetis and Budimir, 2001).

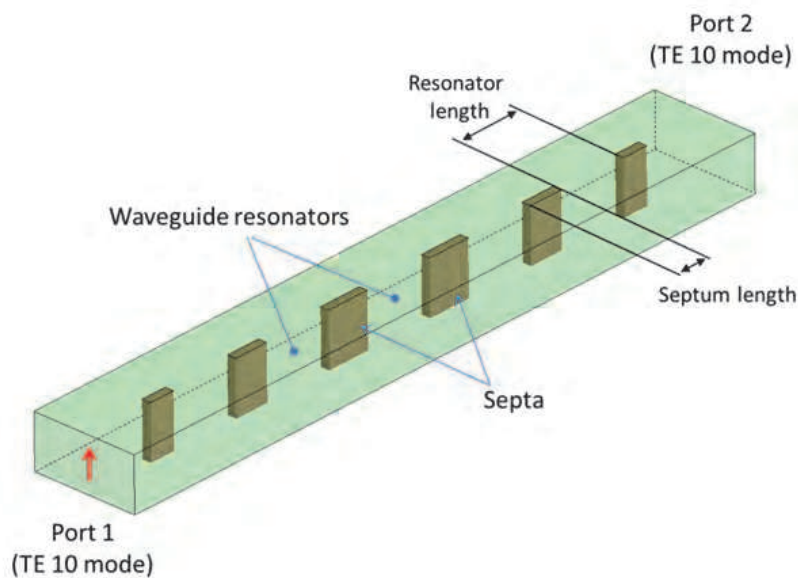


Fig. 4.5. Pass-band filter configuration with *E*-plane septum discontinuities.

The evanescent mode filter is another common structure featuring longitudinal discontinuities (Bornemann and Arndt, et al. 1990). As shown in Fig. 4.6, this configuration is based on a dual ridge waveguide (single ridge versions are also used). Therefore, it leads to more compact implementations in terms of both length and transverse section with respect to the rectangular counterparts. The smaller transverse section also produce a wider attenuation bandwidth. The small gap between the two ridges however generally reduce the power handling of the structure owing to the multipactor phenomenon. The longitudinal discontinuity is represented by the interruption of the ridge. In particular, the envelope of the adopted ridge waveguide is selected so that the TE<sub>10</sub> mode in the discontinuity region is far below cut-off in the operative frequency band. In this way, a strong evanescent-mode discontinuity is created. Besides the dimensions of the ridge waveguide, the relevant parameters for the filter design are the lengths of both the resonators and the evanescent mode sections.

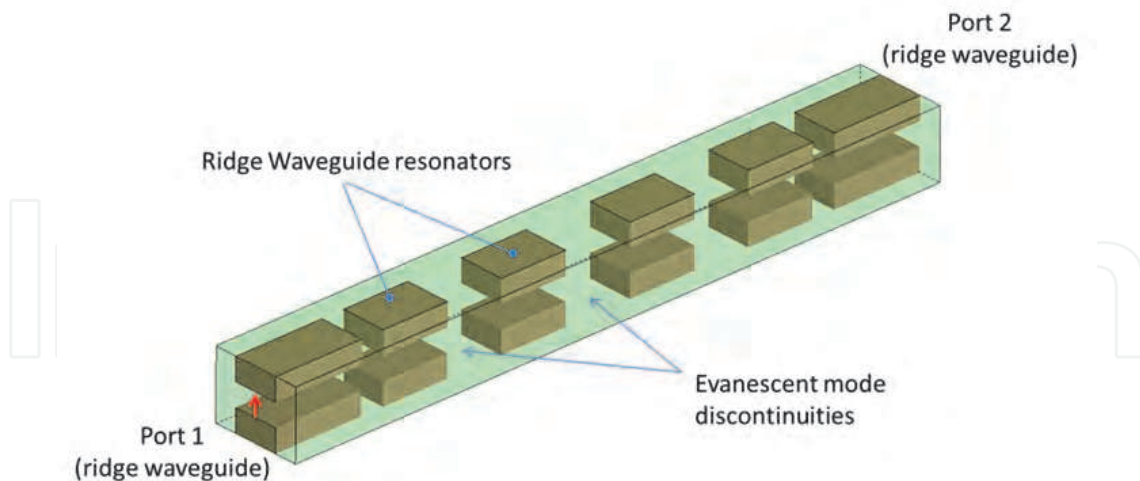


Fig. 4.6. Evanescent mode filter.

As discussed above, all the filter geometries exhibit a large number of design parameters that should be defined according to the required specifications on the frequency response. In the past, this task has been generally accomplished on the basis of synthesis techniques for lumped-parameters circuits and proper transformations (Levy, 1984). However, these techniques do not take into account the frequency dispersion of both the discontinuities and the cavities, the multimodal interactions and the losses which can significantly affect the frequency response of a broadband filter. As a consequence, a considerable optimization work is required to refine the initial solution. In particular, such an approach could lead to sub-optimum designs owing to the presence of local minima in the pertaining cost function. In order to overcome the above-mentioned problems, a design method based on both a distributed-parameter model of the structure and a proper identification technique for the various higher-order spurious effects has been developed (Tascone, et al. 2000). The method exploits the single-mode circuit shown in Fig. 4.2, where each discontinuity is described using its scattering parameters  $S_{11}^{(k)}, S_{21}^{(k)}$  and  $S_{22}^{(k)}$ . In the lossless case, these complex quantities can be conveniently represented using the real parameter  $\gamma_k$  ( $\cos \gamma_k = |S_{11}^{(k)}| = |S_{22}^{(k)}|$  and  $\sin \gamma_k = |S_{21}^{(k)}|$ ) and the phases  $\varphi_{11}^{(k)}$  and  $\varphi_{22}^{(k)}$ . The resonators are instead described using their lengths  $l_k$  and the corresponding waveguide propagation constants  $\beta_k$ . It has been demonstrated that the transmission matrix of the complete circuit can be written as

$$T = \left\{ \prod_{k=1, \dots, n} \begin{bmatrix} \csc \gamma_k & \cot \gamma_k z^{-1} e^{-j\psi_k} \\ \cot \gamma_k & \csc \gamma_k z^{-1} e^{-j\psi_k} \end{bmatrix} \right\} \begin{bmatrix} \csc \gamma_0 & \cot \gamma_0 \\ \cot \gamma_0 & \csc \gamma_0 \end{bmatrix}$$

where  $z^{-1} e^{-j\psi_k} = \exp\{-j[2\beta_k l_k - (\varphi_{11}^{(k-1)} + \varphi_{22}^{(k)})]\}$  and  $\psi_k$  are unknown phase terms which have been introduced in order to allow the synthesis of arbitrary frequency responses and to keep the different phase behavior of the resonators into account. It should be noted that the quantity  $2\beta_k l_k - (\varphi_{11}^{(k-1)} + \varphi_{22}^{(k)})$  is the Round Trip Phase Shift of the resonators. It can be also recognized that the elements of the transmission matrix  $T$  are N-degree polynomials in the complex variable  $z^{-1}$

$$T_{11}(z) = \sum_{k=1}^N a_k z^{-k} \quad \text{and} \quad T_{21}(z) = \sum_{k=1}^N b_k z^{-k}$$

As well-known, these parameters are related to the scattering matrix of the overall filter

$$T_{11} = 1 / S_{11} \quad \text{and} \quad T_{21} = S_{11} / S_{21}$$

In particular, the  $T_{21}$  parameter provides a very convenient description of the frequency response in both the passband (where  $T_{21} \approx S_{11}$ ) and the attenuated bands (where  $T_{21} \approx 1 / S_{21}$ ). Thanks to the polynomial representation, this single parameter can be used to analytically define all the specifications of the filter in the same fashion as antenna arrays and digital filter design techniques (FIR).

Once the polynomial  $T_{21}$  has been defined according to the required specifications, an extraction procedure is applied to determine the scattering matrix of the various discontinuities (Tascone, et al. 2000) and the phase terms  $\psi_k$ . Starting from the electrical parameters, the geometry of the discontinuities e.g. iris apertures, septum lengths are obtained exploiting a pre-computed curve. The length of the various resonators  $l_k$  is also computed exploiting both the  $\psi_k$  and the  $\phi_{11}^{(k-1)} + \phi_{22}^{(k)}$ .

The synthesized geometry is then simulated using a full-wave method (e.g. Peverini, 2004). As expected, the computed full-wave response is different from the synthesized polynomial  $T_{21}$  owing to the neglected phenomena in the synthesis model. Nevertheless, these discrepancies can be properly compensated using the developed identification procedure (Tascone, et al. 2000). Such a technique starts with the interpolation of the full-wave response with a N-degree polynomial

$$A_{21}(z) = \sum_{k=1}^N c_k z^{-k}$$

In this way, the overall procedure from the synthesis scheme to the analysis tool can be represented as a single abstract system having the  $T_{21}(z)$  and  $A_{21}(z)$  polynomials as input and output, respectively. These quantities can be interpreted as periodic signals with  $N$  harmonics. Hence, their coefficients  $b_k$  and  $c_k$  can be considered as the discrete spectra of these input and output signals, respectively. This approach leads to identification of the above mentioned abstract system with a linear system, for which the transfer function  $H(z)$  can be defined as the ratio between the output and input spectra

$$h_k = c_k / b_k$$

The introduced transfer function  $H(z)$  properly models the frequency dispersion of the discontinuities, the multimodal interaction and the losses. Therefore, it can be used to compute the coefficients a new "pre-distorted" frequency response  $T_{21}'(z)$  as

$$b_k' = b_k / h_k$$

Finally, the synthesis scheme discussed above is applied to this "pre-distorted" polynomial  $h_k = c_k / b_k$  to obtain the final filter geometry. Indeed, a single iteration is usually enough for

several considered filter designs. Anyway, some more iterations can be performed in presence of highly-dispersive discontinuities or strong coupling to the evanescent modes. The presented synthesis technique has been generalized to the design of waveguide polarizers (Virone, et al. 2005) and waveguide diplexers (Virone, et al. 2009). For the latter, the frequency response of a relevant design example for Digital Video Broadcasting applications is reported in Fig. 4.7. It has been conceived with the capacitive iris configuration (see Fig. 4.4). With reference to the port numbering reported in Fig. 4.1, the reflection coefficient at common port ( $S_{11}$ ) is below -30 dB for both the TX (10.95-12.75 GHz) and RX (13.75-14.5 GHz) frequency bands. Similar reflection levels have been obtained at both port 2 and 3 for the TX and RX bands, respectively. Due to the metallic losses, the transmission coefficient is about -0.4 dB in the pass-band of both channels (an aluminum prototype has been simulated). The isolation levels  $1/S_{21}$  (from TX to port 1) and  $1/S_{31}$  (from 1 to RX) are higher than 55 dB in the RX and TX band, respectively. A level of 55 dB has been obtained in both bands from TX to RX ( $1/S_{32}$ ) as well.

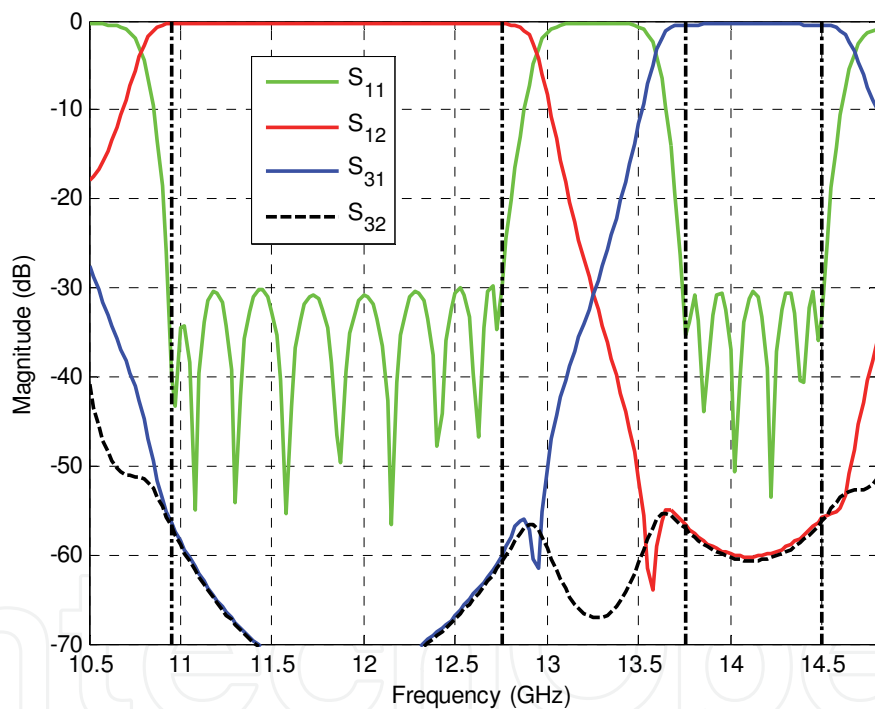


Fig. 4.7. Waveguide diplexer with capacitive irises. The port numbering is reported in Fig. 4.1. The vertical dash-dotted lines represent the TX (10.95-12.75 GHz) and RX (13.75-14.5 GHz) frequency bands.

#### 4.2 Stop-band structures

Strongly resonant waveguide discontinuities are required to design a stop-band filter. In particular, they have to exhibit both a relatively wide transmission zero around the specified stop-band and a moderate reflection level in the pass-band. A very common configuration is the *E*-plane stub in rectangular waveguide shown in Figs. 3.3-3.4. Several discontinuities have to be cascaded to meet the specifications. The number of stubs is mainly related to the

desired isolation level in the given bandwidth. Proper arranging of the various discontinuities is mandatory to avoid degradation of the stop-band performance owing to tunnel phenomena and strong multimode interactions. A significant design example of stub-filter for satellite applications has already been described in section 3. Other designs can be found in (Kirilenko, et al. 1994) and (Levy, 2009).

## 5. Ortho-Mode Transducers

A canonical Ortho-Mode Transducer (OMT) configuration has three physical waveguide ports (see Fig. 5.1). The common port is a metallic waveguide having a two-fold symmetric cross section (e.g. square or circular) which supports two degenerate modes i.e. two orthogonal polarizations. Hence, two electrical ports should in fact be adopted to describe the electromagnetic field at the common port. With reference to Fig. 5.1, the symbols  $V$  ( $H$ ) is hereinafter used to indicate the vertical (horizontal) polarization and Port 1 (2) is referred as the electrical port of the component  $V$  ( $H$ ). The two coupled ports are usually rectangular waveguides operating in the single-mode regime. In other words, the OMT should in fact be described using the four-port scattering matrix shown in Fig. 5.1 (Peverini, et al. 2006).

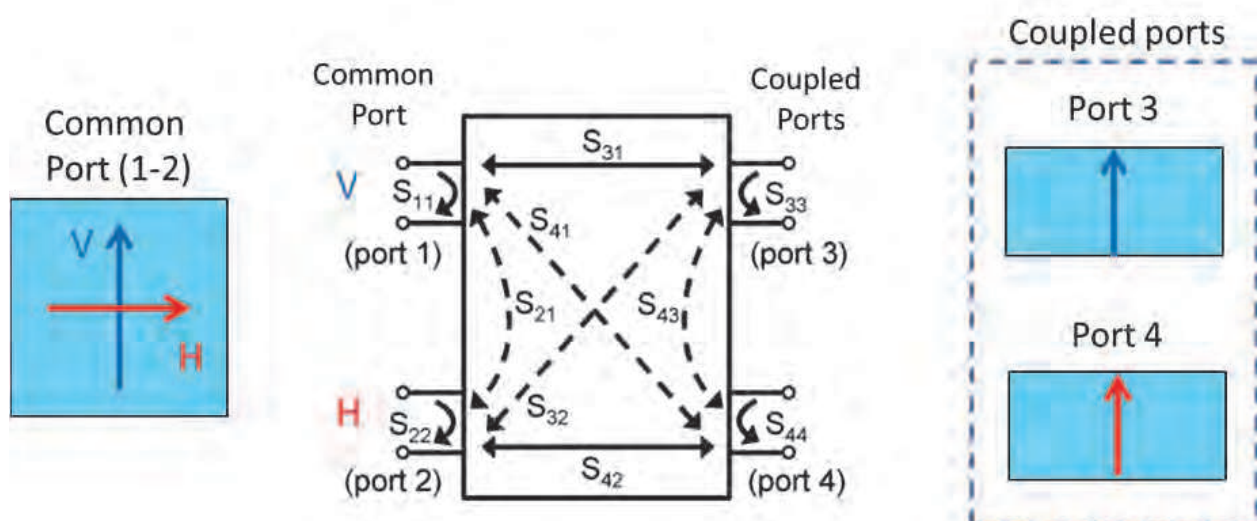


Fig. 5.8. The three waveguide ports of the OMT and the four-port scattering matrix equivalent circuit.

An OMT waveguide architecture is conceived so that each of the two degenerate modes at the common port is nominally coupled to one of the two single-mode ports only. According to Fig. 5.1, Port 3 (4) is the coupled port of the component  $V$  ( $H$ ). It means that the magnitude of the direct scattering parameter  $S_{31}$  ( $S_{42}$ ) should be ideally equal to one. The magnitude of the cross-coupling terms  $S_{41}$  ( $S_{32}$ ) and the isolation terms  $S_{21}$  and  $S_{43}$  should instead be zero.

According to a receive-mode operative condition, an OMT is therefore used to route the two orthogonally polarized field components at the common port to two different waveguide ports. By reciprocity, in transmit mode, an electrical signal excited at one of the two single-mode ports is only routed to one of the two available polarizations at the common port.

The routing of the various signals is obtained introducing suitable apertures and discontinuities between the common waveguide and the coupled waveguides. The isolation

between the two signals pertaining to the orthogonal polarizations is generally obtained exploiting both the symmetry of the structure and particular cut-off phenomena.

Besides the isolation, other figures of merit of the OMT consist in power handling, insertion loss, matching level, and low spurious higher-order-mode excitation at the four electrical ports. Group delay equalization between the V and H channels is also required in some specific applications. All the relevant electrical parameters of the OMT should be robust with respect to the manufacturing tolerances. Manufacturing complexity, compactness and proper orientation of the physical ports are also very important design parameters.

Several OMT configurations can be found in the literature. Their performances can change significantly from both the electromagnetic and mechanical perspectives. The correct choice highly depends on the application, however, it is worth mentioning that this choice strongly affects the overall feed system topology. Therefore, it is important to correctly choose the OMT since it drives the complexity as well as the cost and the dimension of the overall antenna feed system.

The most interesting waveguide configurations for satellite communication systems will be discussed in the following, starting from the basic ones up to the more recent and advanced architectures. For the sake of simplicity, the square-waveguide common-port implementations are only shown i.e. the V (H) polarization shown in Fig. 5.1 corresponds to the TE<sub>10</sub> (TE<sub>01</sub>) mode. Nevertheless, all the presented architectures can in principle be extended to the circular cases.

### 5.1 Standard T-junction or side-coupling OMT

One of the simplest OMT architectures is represented by the T-junction shown in Fig. 5.2 (Schlegel and Fowler, 1984). The TE<sub>10</sub> mode incident at the common port (carrying the vertical polarization) propagates along the main arm (also called common waveguide) and it is coupled to the fundamental mode of the rectangular port 3. The TE<sub>10</sub> in the common waveguide is not coupled to the fundamental TE<sub>10</sub> at port 4 owing to both the symmetry of the structure and the orthogonality of their field distributions.

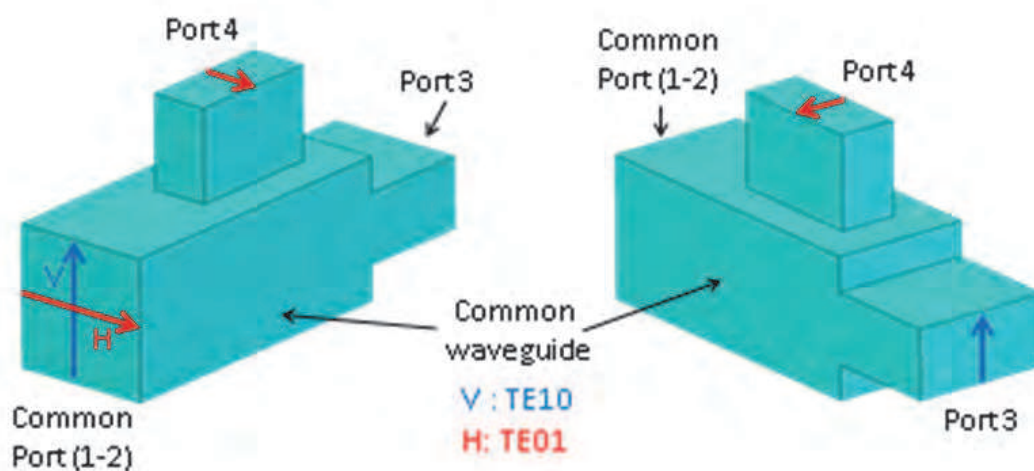


Fig. 5.9. Standard T-junction OMT.

The horizontal polarization, i.e. the TE<sub>01</sub> mode at the common port is instead coupled to the side arm (fundamental mode of port 4) only. Indeed, the same polarization is under cut-off at port 3. As a consequence, ports 3 and 4 are also isolated as far as their fundamental mode is concerned.

A careful design of the various geometrical parameters is required in order to obtain an OMT with a suitable matching level. The side-arm coupling can be also performed on the other orthogonal side of the common waveguide with a different orientation of the coupled waveguide i.e. *E*-plane coupling instead of *H*-plane coupling. Anyway, this simple compact configuration only works in quite narrow frequency bands. Proper matching structures such as septa, irises and steps can be added to enlarge the operative frequency band up to 20% (Dunning, et al. 2009) or to obtain a dual-band component (Rebollar, 1998). However, proper care should be taken in order not to impair the power handling of the structure. Moreover, the bandwidth limit of this configuration is related to the excitation of the higher order modes TE<sub>11</sub> and TM<sub>11</sub> owing to the one-fold symmetry of the structure.

## 5.2 Boifot OMT

The Boifot junction has been introduced in order to obtain an OMT with a large operative bandwidth (Boifot, 1990). As can be seen in Fig. 5.3, a symmetric *E*-plane coupling is exploited for the horizontal polarization in order to obtain a two-fold symmetry of the whole structure. This feature avoids the excitation of the TE<sub>11</sub> and TM<sub>11</sub> higher-order modes in the common waveguide. In this way, the operative frequency band of the device can be extended above the cutoff frequency of these modes up to the TE<sub>20</sub> cutoff. The two symmetric side arms have to be combined using both straight and bent rectangular waveguide sections to obtain a single signal at port 4. The corresponding structure is therefore more complex than an OMT with a single side arm.

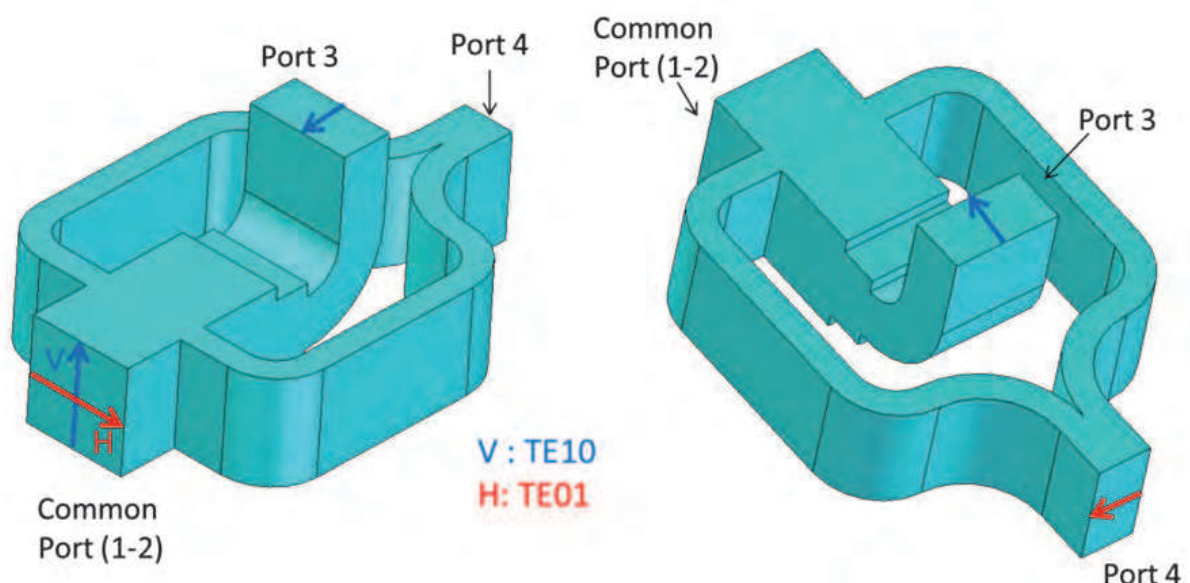


Fig. 5.10. Scheme of the Boifot OMT.

A septum (not shown) is also inserted in the common waveguide, between the coupling apertures and the stepped transition to port 3, in order to improve the matching of the H-polarization. The septum is oriented to allow the direct routing of the vertical polarization to port 3. In the original configuration, metallic posts were also inserted in the coupling apertures of the two side arms (Boifot, 1990).

It has been shown in the literature that large matching and isolation bandwidths (30%) can be obtained using this configuration. The main drawbacks consist in the manufacturing complexity and large size of the OMT. It should be pointed out that a differential error in the length of the two waveguides of the combination structure (owing to manufacturing uncertainties) can destroy the symmetry of structure with a consequent reduction of the isolation performance. Moreover, the insertion loss and group delay are intrinsically very different for the two polarizations.

### 5.3 Turnstile junctions

The turnstile junction (Navarrini and Plambeck, 2006) exploits a symmetric E-plane coupling for both polarizations. With reference to Fig. 5.4, the vertical polarization is only coupled to the fundamental TE<sub>10</sub> mode at both Port 3 and Port 3'. The same polarization would also couple to the TE<sub>01</sub> mode at ports 4 and 4'. However, this mode is under cut-off in the operative frequency range of the structure. The horizontal polarization is instead coupled to both Port 4 and 4'. It should be noted that in the E-plane coupling, the symmetric ports exhibit an opposite orientation of the electric field.

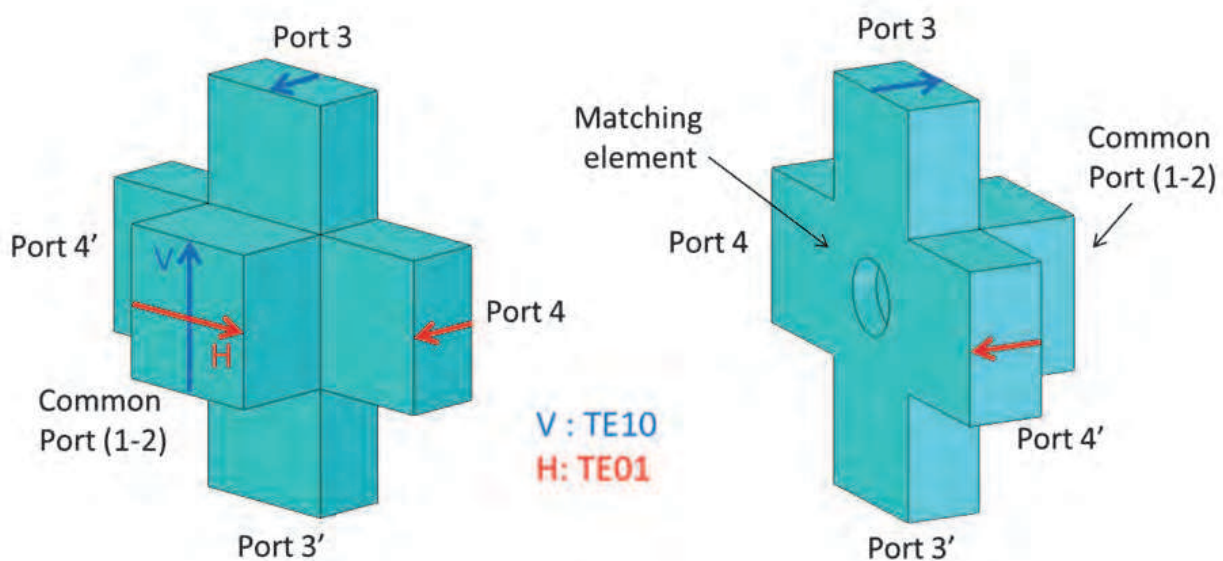


Fig. 5.11. The turnstile junction.

This turnstile junction does not excite the TE<sub>11</sub> and TM<sub>11</sub> modes in the common waveguide. Therefore, the upper limit of the frequency band is related to the cutoff frequency of the TE<sub>20</sub> mode and to the cutoff frequency of the TE<sub>01</sub> mode at the coupled ports.

A proper protrusion with either pyramidal, cylindrical or parallelepiped shape should be introduced in the back of the junction (see Fig. 5.4) in order to improve the matching.

The turnstile junction exhibits the same insertion loss and group delay for both polarizations since the latter undergo a symmetric coupling at the same section of the common port. As a drawback, two different waveguide structures (not shown) are required to combine the opposite ports. Even in this case, possible asymmetries of the combiners owing to the manufacturing uncertainties should be managed to avoid isolation problems.

This OMT type can operate in a large frequency band (more than 30%) with good power handling properties. However, the presence of two combiners make this configuration less compact and with higher losses with respect to the previous solutions.

#### 5.4 Orthomode Junctions (OMJ)

In the case of dual-band dual-polarization feed systems where the transmit and receive bands are suitably separated, an interesting configuration is represented by the so called orthomode junction (OMJ) (Garcia, et al., 2010). Similarly to the turnstile junction, the OMJ also exploits a symmetric coupling section for both polarizations. A simplified H-plane implementation is shown in Fig. 5.5. The OMJ however exhibits a secondary common port in square (or circular) waveguide. Such a waveguide is below cut-off at the lower frequencies. Therefore, the low-band signals can be properly reflected and coupled to the side ports. Two combiners are required to obtain a single port for each polarization. It should be noted that the absence of a proper matching element in the common port leads to a quite narrow matching bandwidth for the side-coupled signals.

As far as the high-band is concerned, the complete OMT should be equipped with proper stop-band filters (not shown) on the side arms in order to prevent leakage of the high-frequency signals from the side ports. In this way, both polarizations are routed to the secondary common port. The latter can be now separated using another single-band OMT (not shown).

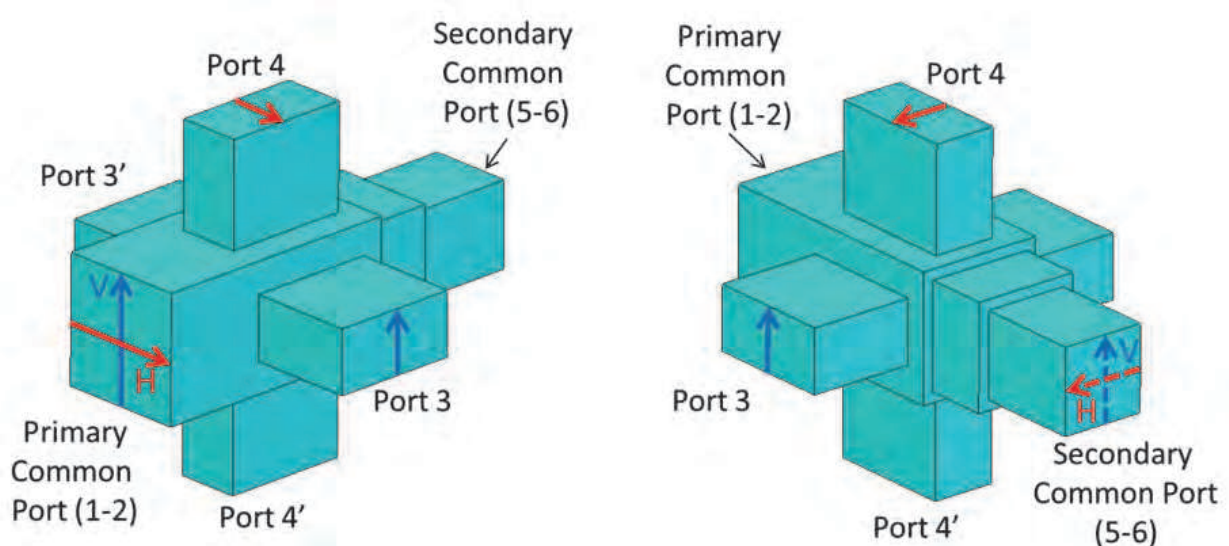


Fig. 5.12. Scheme of an Ortho-Mode Junction (OMJ).

The OMT configuration of Fig. 5.5 can be referred as a self-diplexing structure. This kind of components is very important in order to reduce the overall number of antennas on the payload. As a matter of fact, besides the narrow bandwidth, this added functionality leads to increased complexity, size and losses of the device.

### 5.5 Reverse coupling OMT

The broadband operative condition of some of the above-mentioned OMTs is mainly obtained inserting proper matching elements such as septa, irises or other protruding objects in the common waveguide. Besides the increased manufacturing complexity, the presence of these matching structures can limit the power handling capability of the OMT. An alternative solution to obtain broad-band OMTs has therefore been presented in (Peverini, et al., 2006). The core of the device shown in Fig. 5.6 consists in a reverse coupling section. As far as the vertical polarization is concerned, the signal in the common waveguide is coupled to the adjacent parallel rectangular waveguide by means of the E-plane apertures. This operation, which resembles the working principle of a branch-guide directional coupler, has been schematized in Fig. 5.7.

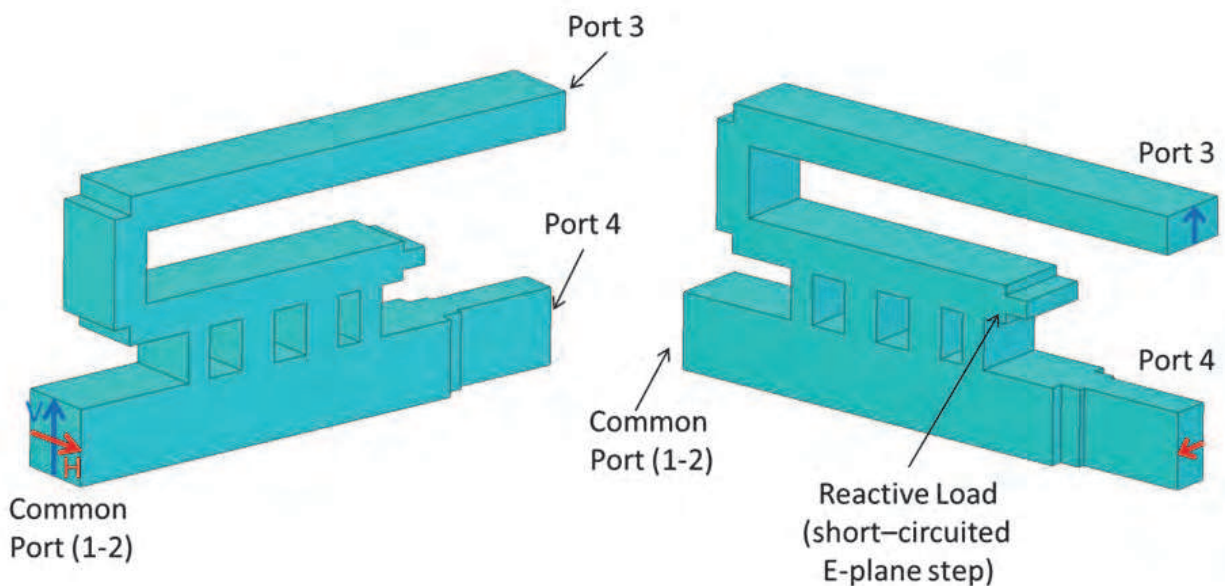


Fig. 5.13. Reverse-coupling OMT.

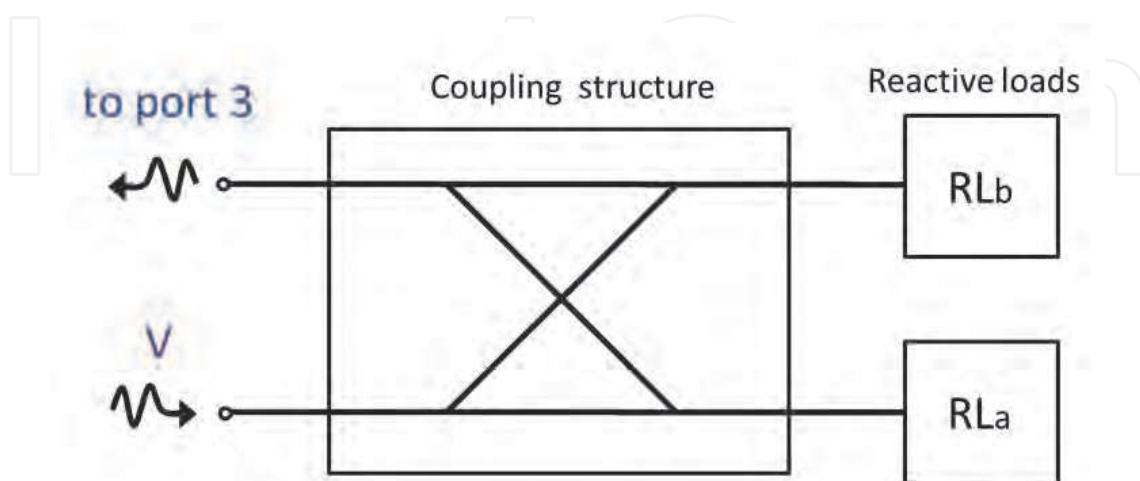


Fig. 5.14. Network representation of the reverse coupling structure for the V-polarization.

Such a directional coupler is loaded with two reactive impedances  $RL_a$  and  $RL_b$  representing the stepped transition to Port 4, which is under cut-off for the vertical polarization, and the short-circuited E-plane step on the coupled rectangular waveguide, respectively. The complete structure is properly designed so that the various coupled and reflected contributions produce a constructive interference (in-phase combination) for the  $V$ -signal to port 3. On the contrary, a destructive interference phenomenon is instead exploited to obtain a low-reflection coefficient at both common and coupled ports (Peverini, et al., 2006). The reverse-coupling section and the stepped transition to port 4 should also be designed in order to route the horizontal polarization to port 4 with a low reflection coefficient. The  $180^\circ$  bend and the subsequent straight rectangular waveguide section in Fig. 5.6 allow a proper alignment between port 3 and port 4. Furthermore, stepped waveguide twist (Baralis, et al., 2005) can be introduced to provide the same orientation of the two ports. It should be noted that the reverse coupling structure can also be adopted to either provide a symmetric coupling structure (Navarrini and Nesti, 2009) which allow a larger operative frequency range or to design a self-diplexing unit with a more controlled broadband coupling with respect to the canonical OMJ.

## 6. Corrugated horns

A corrugated horn is the most employed illuminator for parabolic, offset or Cassegrain configurations in satellite feed system for its excellent potential dual polarized characteristics. The first studies on these antennas date back to the pioneer works of Clarricoats and Olver (Clarricoats and Olver, 1984). This antenna configuration originates from the theoretical study of the modes of a cylindrical waveguide where the metallic walls are substituted by a surface impedance. If specific impedance conditions are considered, the structure can support a particular hybrid mode, known as  $HE_{11}$ , whose field components, if it radiates, minimize cross polarization level. It has been shown that this particular surface condition can be realized by means of  $\lambda/4$  depth corrugations. To excite this mode a suitable transition between the smooth circular waveguide and the corrugated one is necessary. This can be obtained in two ways as shown in Fig. 6.1, i.e. by means of depth corrugation increment up to the desired  $\lambda/4$  value (Fig. 6.1a) or a depth corrugation decrement from the value  $\lambda/2$  up to  $\lambda/4$  (Fig. 6.1b). The second configuration permits wide band performances and for this reason it is usually employed. In order to satisfy the radiation pattern requirements in terms of half power beamwidth and field taper at a specific illumination angle, the radiating cross section has to be much larger than the input monomodal waveguide and therefore a suitable radius transition is necessary. The radius profile as well as the corrugations geometry are free design parameters which has to be chosen in order to match the structure and, at the same time, perform the desired conversion of the incident field to the  $HE_{11}$ -like mode. Since the number of corrugations can be of the order of hundreds, the design is quite complicate in particular for wideband application where also the antenna compactness is often required.

A part few works which gives some useful design criteria and design map (Granet et al., 2005), the standard approach in the technical literature is based on the employment of a particular radius profile as a starting point for global optimization schemes (Jamnejad et al., 2004). In this respect, the so called dual-profile circular corrugated horn (DPCCH) is usually regarded as the state of the art. This profile consists of a combination of a sine square law

and an exponential function joined by a smooth transition (see Fig.6.2). The other geometrical parameters, i.e. the dimensions and reciprocal distances of each corrugation, are usually chosen in accordance to empirical/semi analytical formulas. Although the performances obtained in this way are generally interesting, they cannot meet the specifications in the case of high performance wideband systems. For this reason global optimization algorithms (e.g. particle swarm optimization or genetic algorithms) are used not only as simple refinement tools but as a way to actually define the whole antenna geometry. The relevant drawbacks are related not only to the quite long computation times required but, mainly, to the design itself. Indeed, quite often the initial smoothness of the DPCCH profile is completely lost, which turns into a high sensitivity of the electromagnetic performances to the mechanical tolerances.

Recently a suitable design strategy has been proposed (Addamo et al. , 2010) for circular corrugated horn and here briefly described. Roughly speaking, from a functional point of view the first group of corrugations (called "throat region") in the horn is designed in order to convert the input incident field into the  $HE_{11}$ -like mode. The remaining part (called "radiating region") modifies this field configuration in order to guarantee the desired radiation pattern specifications (see Fig.6.3). The idea, then, is to separate the design of the throat and radiating regions by applying the most appropriate technique for each. As far as the radiating region is concerned, since the radius variation between two adjacent horn corrugations is usually relatively small, a companion periodic structure can be used (see Fig. 6.4). The desired field configuration can be then interpreted as a particular Bloch wave and the design can be obtained exploiting the periodic structure theory. The throat region definition is much more complicate since it has to perform a suitable mode conversion from the input  $TE_{11}$  to the desired  $HE_{11}$ -like mode. However since the radiating region is defined in the previous design step, this part can be obtained by means of a guided parametric analysis and therefore optimization techniques can be employed just as a refinement.

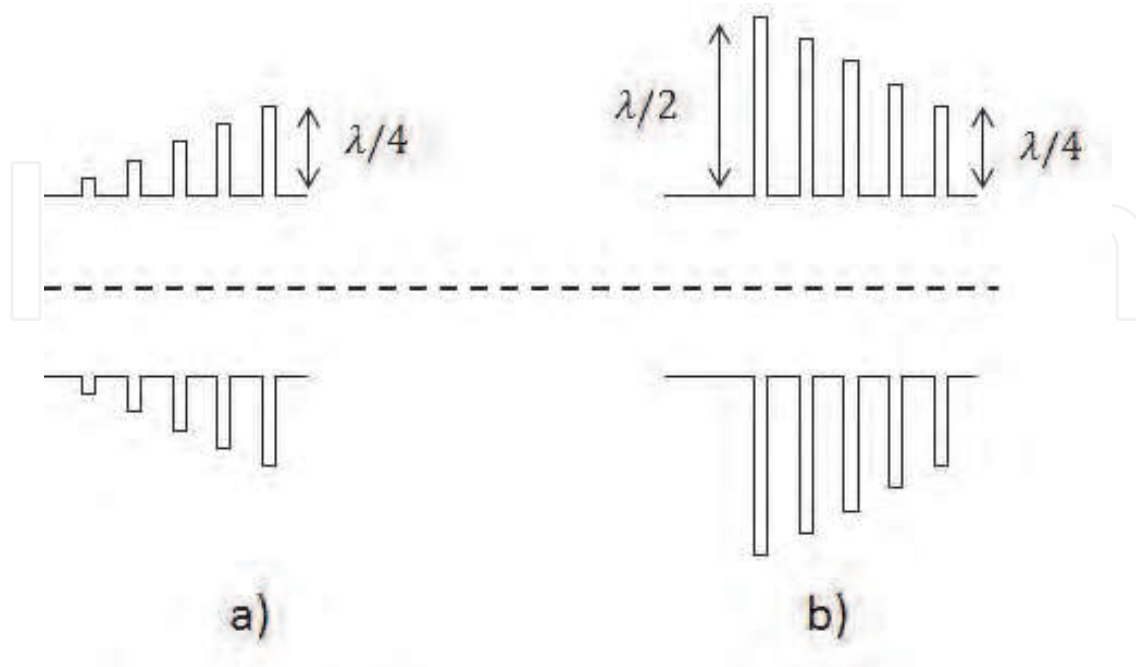


Fig. 6.15. Transitions from circular to corrugated waveguide.

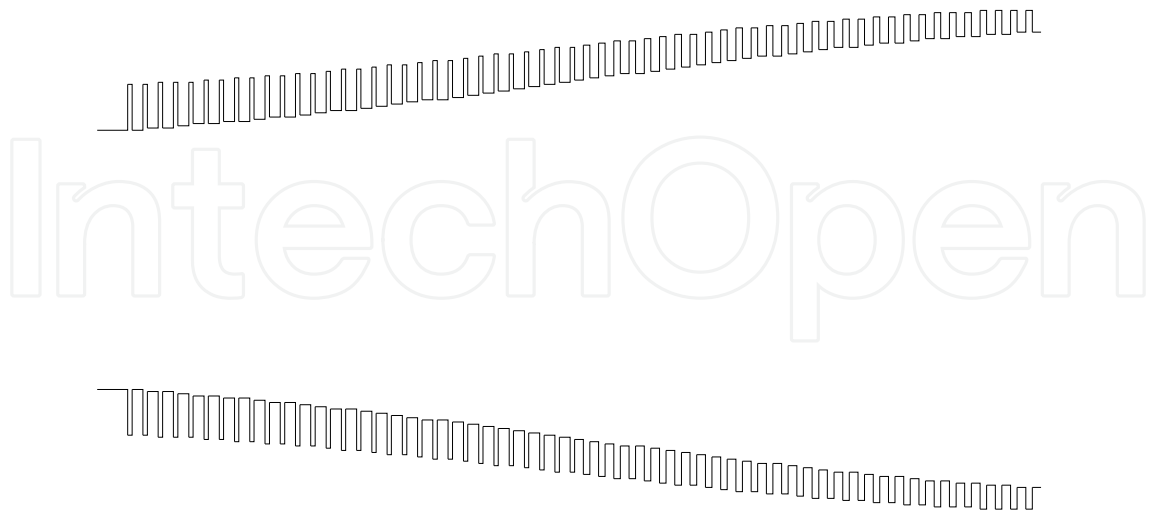


Fig. 6.2. An example of Dual Circular Corrugated Horn Profile (DPCCH).

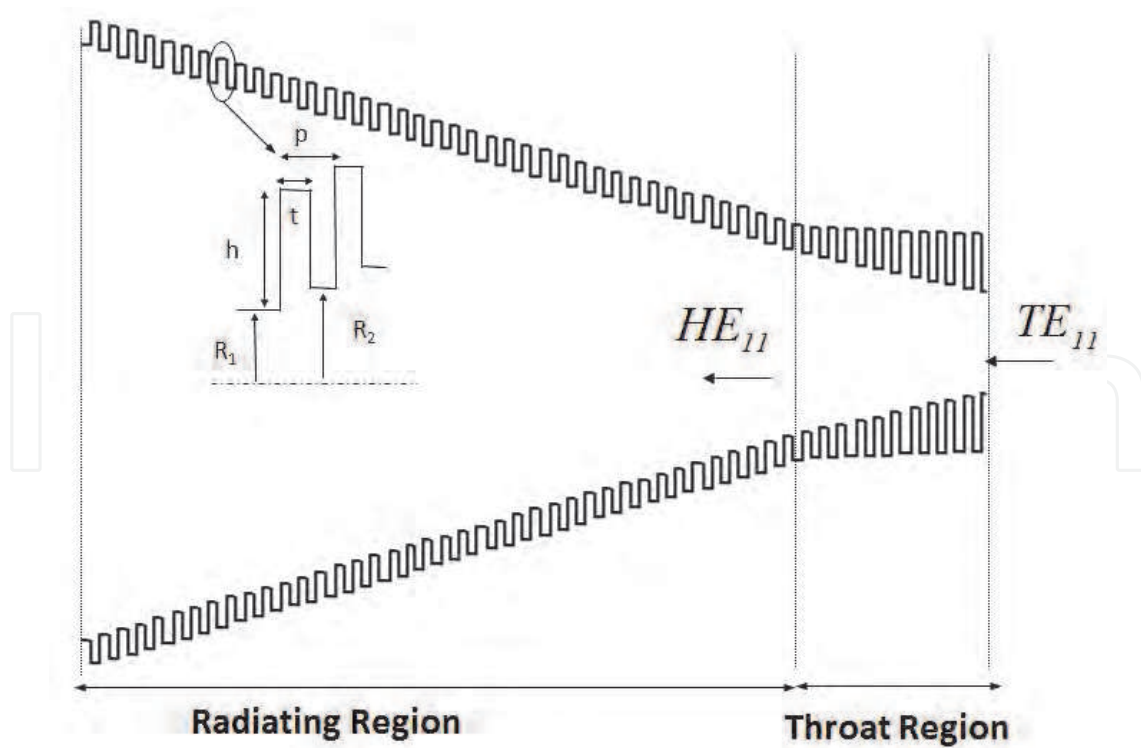


Fig. 6.3. Throat and radiating regions.

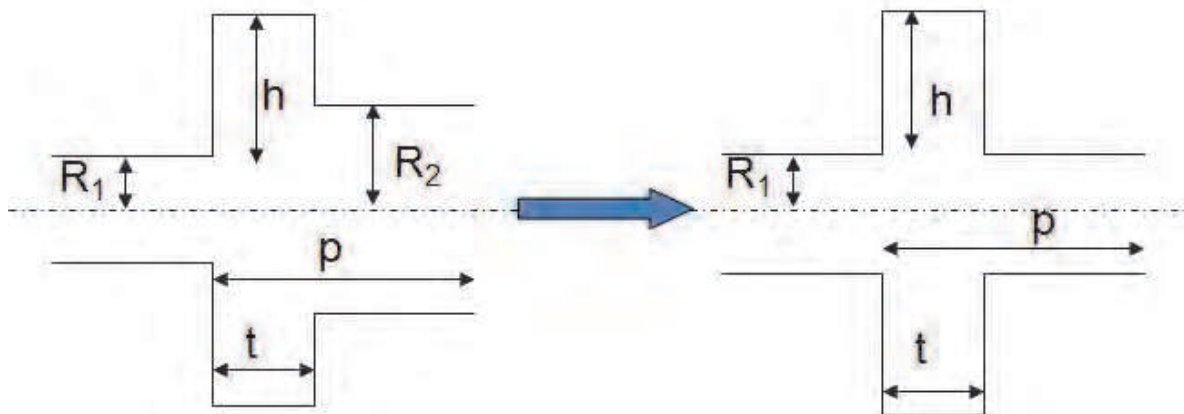


Fig. 6.4. Companion periodic structure.

## 7. References

- Addamo G., Peverini O.A., Virone G., Tascone R., Orta R. and Cecchini P., "A Ku-K Dual-Band Compact Circular Corrugated Horn for Satellite Communications", *IEEE Antennas and Wireless Propagation Letters: Volume 8*, 2009, Page(s):1418 - 1421
- Addamo G., Peverini O.A., Tascone R., Virone G., Cecchini P., Mizzoni R. and Orta R., "Dual use Ku/K band Corrugated Horn for Telecommunication Satellite", *European Conference on Antennas and Propagation (EUCAP)*, Barcelona (Spain) 2010
- Anza S., Vicente C., Raboso D., Gil J., Gimeno B., & Boria V. E. (2008), Enhanced Prediction of Multipaction Breakdown in Passive Waveguide Components Including Space Charge Effects, *Proceedings of the 2008 IEEE International Microwave Symposium*, Atlanta (U.S.), pp. 1095- 1098, June 2008
- Arndt F., Beyer R., Reiter J.M., Sieverding, T., Wolf, T., "Automated design of waveguide components using hybrid mode-matching/numerical EM building-blocks in optimization-oriented CAD frameworks-state of the art and recent advances", *IEEE Transactions on Microwave Theory and Techniques*, Vol. 45, Issue 5, May 1997, pp. 747-760
- Baralis, M., Tascone, R., Olivieri, A., Peverini, O.A., Virone, G., Orta, R., "Full-wave design of broad-band compact waveguide step-twists", *IEEE Microwave and Wireless Components Letters*, Vol. 15, Issue 2, Feb. 2005, pp. 134-136
- Beniguel Y., Berthon A., Klooster C.V., Costes L., "Design realization and measurements of a high performance wide-band corrugated horn", *IEEE Transactions on Antennas and Propagation*, Volume 53, Issue 11, Page(s) 3540 - 3546, Nov. 2005

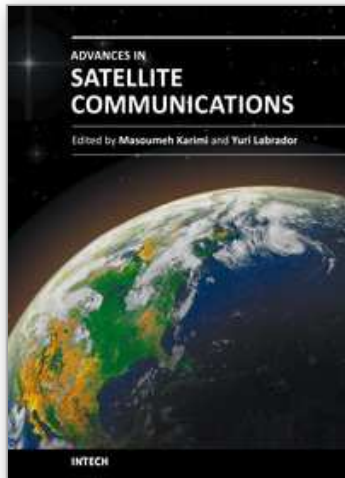
- Boifot A.M., Lier E., Schaug-Pettersen T., "Simple and broadband orthomode transducer", IEEE Proceedings, Vol. 137, Pt. H, No. 6, Dec 1990, pp. 396-400
- Bornemann J., Arndt F., "Transverse Resonance, Standing Wave, and Resonator Formulations of the Ridge Waveguide Eigenvalue Problem and Its Application to the Design of E-Plane Finned Waveguide Filters", IEEE Transactions On Microwave Theory And Techniques, Vol. 38, No. 8, August 1990
- Cecchini P., Mizzoni R., Ravanelli R., Addamo G., Peverini O.A., Tascone R. and Virone G., "Wideband Diplexed Feed Chains for FSS + BSS Applications", EuCAP Conference 2009, Berlin (Germany), Page(s):3095 - 3099
- Cecchini P., Mizzoni R., Ravanelli R., Addamo G., Peverini O. A., Tascone R., & Virone G. (2010), Ku/K Band Feed System for Satellite Applications, Proceedings of the 32nd ESA Antenna Workshop, ESTEC, Noordwijk (Netherlands), Oct.2010
- Clarricoats P. J. B., Olver A.D., Corrugated Horn for Microwave Antennas, Peter Peregrinus Ltd, London (UK), 1984.
- Dunning A., Srikanth S., Kerr A. R. "A Simple Orthomode Transducer for Centimeter to Submillimeter Wavelengths", 20th International Symposium on Space Terahertz Technology, Charlottesville, 20-22 April 2009, pag. 191-194
- European Space Agency (2007), Multipactor Calculator, Available from <<http://multipactor.esa.int/>>
- Garcia R., Mayol F., Montero J. M, Culebras. A. "Circular Polarization Feed with Dual Frequency OMT based on Turnstile junction", IEEE Antennas and Propagation Society International Symposium, 2010, 11-17 July 2010
- Goussetis G. and Budimir D., "E-Plane Double Ridge Waveguide Filters and Diplexers for Communication Systems", European Microwave Conference, 2001, 31st Oct. 2001, Page(s):1-4
- Granet C., and James G. L., "Design of corrugated horns: A primer, IEEE Antennas and Propagation Magazine, vol. 47, no. 2, pp. 76-84, April 2005.
- Hartwanger C., Gehring R., Hong U., Wolf H. and Drioli L.S., "A Dual Polarized Wide Band Feed Chain for FSS and BSS Satellite Services", EuCAP 2007 conference, Page(s)1 - 6, Nov. 2007
- Jamnejad V., and Hoorfar A., "Design of corrugated horn antennas by evolutionary optimization techniques", IEEE Antennas and Wireless Propagation Letters, vol. 3, 2004, pp. 276-279.
- Kirilenko A. A., Rud L. A. , Senkevich S. L. ,"Spectral Approach to the Synthesis of Bandstop Filters", IEEE Trans. Microwave Theory Tech., vol.42, no.7, Jul. 1994, pp. 1387-1392
- Levy R., Cohn, S. B., "A History of Microwave Filter Research, Design, and Development", IEEE Trans. Microwave Theory Tech., vol.32, no.9, Sep. 1984, pp. 1055-1067
- Levy, R. , "Compact Waveguide Bandstop Filters for Wide Stopbands", IEEE MTT-S International Microwave Symposium Digest, 2009, 7-12 June 2009, pp. 1245-1248
- Lui P.L., "Passive intermodulation interference in communication systems", Electronics & Communication Engineering Journal, Vol. 2 Jun 1990, Page(s) 109-118
- Navarrini A. and Plambeck R. L. , "A Turnstile Junction Waveguide Orthomode Transducer", IEEE Transactions on Microwave Theory and Techniques, Volume : 54, Issue:1 , Jan. 2006 pp. 272-277

- Navarrini A., Nesti R., "Symmetric Reverse-Coupling Waveguide Orthomode Transducer for the 3-mm Band", *IEEE Transaction on Microwave Theory and Techniques*, Vol. 57, No. 1, Jan 2009, pp. 80-88
- Parikh K. S., Singh D. K., Praveen Kumar A., Rusia S., & Sangeetha K. (2003), Multi-Carrier Multipactor Analysis of High Power Antenna Tx-Tx Diplexer for SATCOM Applications, *Proceedings of the 4th International Workshop on Multipactor, Corona and Passive Intermodulation in Space RF Hardware*, ESTEC, Noordwijk (Netherlands), Sept. 2003
- Peaverini O. A., Tascone R., Baralis M., Virone G., Trincherro D. and Orta R., "Reduced-Order Optimized Mode-Matching CAD of Microwave Waveguide Components", *IEEE Trans. Microwave Theory Tech.*, vol.52, no.1, Jan. 2004, pp. 311-318;
- Peaverini O. A., Tascone R., Virone G., Olivieri A., Orta R., "Orthomode Transducer for Millimeter-Wave Correlation Receivers", *IEEE Transactions on Microwave Theory and Techniques*, Vol. 54, No. 5, May 2006, pp. 2042-2049
- Peaverini O.A., Tascone R., Virone G., Addamo G., Olivieri A. and Orta R., "C-Band Dual-Polarization Receiver for the Sardinia Radio-Telescope", *International Conference on Electromagnetics in Advanced Applications (ICEAA09)*, 2009, Turin (Italy), Page(s):186 - 187;
- Rebollar, J.M.; Esteban, J.; De Frutos, J.; "A dual frequency OMT in the Ku band for TT&C applications", *IEEE Antennas and Propagation Society International Symposium*, 1998, Vol 4, 1998, pp. 2258 - 2261
- Rozzi T. E., "Equivalent Network for Interacting Thick Inductive Irises", *IEEE Transactions on Microwave Theory and Techniques*, May 1972, Vol. 20, Issue 5, pp. 323-330
- Schlegel H., Fowler W.D., "The ortho-mode transducer offers a key to polarization diversity in EW systems", *Microwave System News*, September 1984, pp.65-70
- Tascone R., Savi P., Trincherro D., Orta R., "Scattering Matrix Approach for the Design of Microwave Filters", *IEEE Trans. Microwave Theory Tech.*, vol.48, no.3, Mar. 2000, pp. 423-429
- Tienda C., Pérez A. M., Vicente C., Coves A., Torregrosa G., Sánchez J. F., Barco R., Gimeno B., & Boria V. E. (2006), Multipactor Analysis in Coaxial Waveguides, *Proceedings of the IEEE Mediterranean Electrotechnical Conference*, Benalmádena Spain, pp. 195-198, May 2006
- Vahldieck R., Bornemann J., Arndt F.; Grauerholz D., "Optimized Waveguide E-plane Metal Insert Filters For Millimeter-wave Applications", *IEEE Transactions on Microwave Theory and Techniques*, Vol. 31, Issue 1, Jan. 1983, pp. 65-69
- Virone, G.; Tascone, R.; Baralis, M.; Peaverini, O.A.; Olivieri, A.; Orta, R., "A novel design tool for waveguide polarizers", *IEEE Trans. Microwave Theory Tech.*, vol.53, no.3, Part 1, Mar. 2005, pp. 888-894
- Virone G., Tascone R., Baralis M., Olivieri A., Peaverini O. A., Orta R., "Five-Level Waveguide Correlation Unit for Astrophysical Polarimetric Measurements", *IEEE Transactions on Microwave Theory and Techniques*, Volume: 55, Issue: 2, Part 1, 2007, pp. 309 - 317

- Virone G., Tascone, R., Peverini, O.A., Addamo, G., Orta, R., "Combined-Phase-Shift Waveguide Polarizer", IEEE Microwave and Wireless Components Letters, 2008, Vol. 18, Issue 8, Page(s) 509 - 511
- Virone G., Tascone, R., Peverini, O.A., Addamo, G., Orta, R., "Synthesis of wideband waveguide diplexers", Proceeding of the International Conference on Electromagnetics in Advanced Applications, 2009. ICEAA 2009, pp. 459 - 460

IntechOpen

IntechOpen



## **Advances in Satellite Communications**

Edited by Dr. Masoumeh Karimi

ISBN 978-953-307-562-4

Hard cover, 194 pages

**Publisher** InTech

**Published online** 27, July, 2011

**Published in print edition** July, 2011

Satellite communication systems are now a major part of most telecommunications networks as well as our everyday lives through mobile personal communication systems and broadcast television. A sound understanding of such systems is therefore important for a wide range of system designers, engineers and users. This book provides a comprehensive review of some applications that have driven this growth. It analyzes various aspects of Satellite Communications from Antenna design, Real Time applications, Quality of Service (QoS), Atmospheric effects, Hybrid Satellite-Terrestrial Networks, Sensor Networks and High Capacity Satellite Links. It is the desire of the authors that the topics selected for the book can give the reader an overview of the current trends in Satellite Systems, and also an in depth analysis of the technical aspects of each one of them.

### **How to reference**

In order to correctly reference this scholarly work, feel free to copy and paste the following:

Oscar Peverini, Giuseppe Virone, Riccardo Tascone and Giuseppe Addamo (2011). Passive Microwave Feed-Chains for High-Capacity Satellite Communications Systems, *Advances in Satellite Communications*, Dr. Masoumeh Karimi (Ed.), ISBN: 978-953-307-562-4, InTech, Available from:

<http://www.intechopen.com/books/advances-in-satellite-communications/passive-microwave-feed-chains-for-high-capacity-satellite-communications-systems>

**INTECH**  
open science | open minds

### **InTech Europe**

University Campus STeP Ri  
Slavka Krautzeka 83/A  
51000 Rijeka, Croatia  
Phone: +385 (51) 770 447  
Fax: +385 (51) 686 166  
[www.intechopen.com](http://www.intechopen.com)

### **InTech China**

Unit 405, Office Block, Hotel Equatorial Shanghai  
No.65, Yan An Road (West), Shanghai, 200040, China  
中国上海市延安西路65号上海国际贵都大饭店办公楼405单元  
Phone: +86-21-62489820  
Fax: +86-21-62489821

© 2011 The Author(s). Licensee IntechOpen. This chapter is distributed under the terms of the [Creative Commons Attribution-NonCommercial-ShareAlike-3.0 License](#), which permits use, distribution and reproduction for non-commercial purposes, provided the original is properly cited and derivative works building on this content are distributed under the same license.

IntechOpen

IntechOpen